Lehigh University
Lehigh Preserve

Theses and Dissertations

2016

A Coupled Lattice Boltzmann-Extended Finite Element Model for Fluid-Structure Interaction Simulation with Crack Propagation

Wesley J. Keller
Lehigh University

Follow this and additional works at: http://preserve.lehigh.edu/etd

 Part of the Computational Engineering Commons, and the Mechanical Engineering Commons

Recommended Citation
Keller, Wesley J., "A Coupled Lattice Boltzmann-Extended Finite Element Model for Fluid-Structure Interaction Simulation with Crack Propagation" (2016). *Theses and Dissertations*. 2658.
http://preserve.lehigh.edu/etd/2658

This Thesis is brought to you for free and open access by Lehigh Preserve. It has been accepted for inclusion in Theses and Dissertations by an authorized administrator of Lehigh Preserve. For more information, please contact preserve@lehigh.edu.

A Coupled Lattice Boltzmann-Extended Finite Element Model for Fluid-Structure Interaction Simulation with Crack Propagation

by

Wesley John Keller

A Thesis
Presented to the Graduate and Research Committee
of Lehigh University
in Candidacy for the Degree of
Master of Science
in
Computational and Engineering Mechanics

Lehigh University
Bethlehem, Pennsylvania

November 2015

© 2015 Copyright

Wesley John Keller

Thesis is accepted and approved in partial fulfillment of the requirements for the Master of Science in the Department of Mechanical Engineering and Mechanics.

A Coupled Lattice Boltzmann-Extended Finite Element Model for Fluid-Structure Interaction Simulation with Crack Propagation

Wesley John Keller

_____

Date

_____

Thesis Advisor: Dr. Yaling Liu

_____

Department Chair: Dr. Gary Harlow

ACKNOWLEDGEMENTS

The research presented in this thesis was sponsored by Lehigh University's Center for Advanced Technology for Large Structural Systems (ATLSS), and through support from the National Science Foundation (grant nos. CBET-113040 and CBET-1067502) and the National Institutes of Health (grant no. EB015105). Findings and conclusions are those of the author and do not necessarily reflect the views of the sponsors.

The author would like to sincerely thank his thesis advisor Dr. Yaling Liu and collaborator Dr. Jifu Tan for their instrumental contributions to this work.

This work is dedicated to my wife and daughter.

TABLE OF CONTENTS

LIST OF FIGURES

ABSTRACT

Fatigue cracking of structures in fluid-structure interaction (FSI) applications is a pervasive issue that impacts a broad spectrum of engineering activities, ranging from large-scale ocean engineering and aerospace structures to bio-medical prosthetics. Fatigue is a particular concern in the offshore drilling industry where the problem is exacerbated by environmental degradation, and where structural failure can have substantial financial and environmental ramifications. As a result, interest has grown for the development of structural health monitoring (SHM) schemes for FSI applications that promote early damage detection. FSI simulation provides a practical and efficient means for evaluating and training SHM approaches for FSI applications, and for improving fatigue life predictions through robust parametric studies that address uncertainties in both crack propagation and FSI response. To this end, this paper presents a numerical modeling approach for simulating FSI response with crack propagation. The modeling approach couples a massively parallel lattice Boltzmann fluid solver, executed on a graphics processing unit (GPU) device, with an extended finite element (XFE) solid solver. Two-way interaction is provided by an immersed boundary coupling scheme, in which a Lagrangian solid mesh moves on top of a fixed Eulerian fluid grid. The theoretical basis and numerical implementation of the modeling approach are presented, along with a simple demonstration problem involving subcritical crack growth in a flexible beam subject to vortex-induced vibration.

CHAPTER 1

INTRODUCTION

1.1 MOTIVATION

Fatigue cracking of structures in fluid-structure interaction (FSI) applications is a pervasive issue that impacts a broad spectrum of engineering activities, ranging from large-scale ocean engineering and aerospace structures to biomedical prosthetics. The driving mechanism for fatigue failure in FSI applications can be extraneously-induced excitation (an example of which is shown in Figure 1.1 where a stress concentration in the steel shaft of a power generation buoy led to fatigue failure under wave loading), vortex-induced vibration (which impacts submerged pipelines (Huang, 2012)), and/or movement-induced excitation (which has caused problems for flexible components in the aerospace (Cecrdle, 2015) and biomedical fields (Jacobs et al. 2003)).

Fatigue failure is a particular concern in the offshore drilling industry where structural failure can have substantial financial and environmental ramifications, including the cessation of production operations and the spillage of hazardous pollutants. An illustrative example is the fatigue vulnerability of deep water risers for offshore floating production platforms. As shown in Figure 1.2, risers are conduits, generally constructed using a steel or aluminum alloy, that connect the production platform with its network of subsea wellheads for petroleum or natural gas extraction. Risers can be several hundred to several thousand meters in length (for ultra-deep water exploration) and are subject to

flow-induced vibration from chaotic sea motion, wave loading of the platform, and vortex-induced vibration. As a result, risers are subject to high-cycle cyclic loading, as well as environmental degradation from the corrosive marine environment.

In recent years, structural health monitoring (SHM) approaches have been investigated for early identification of riser damage, so that repairs can be made in advance of a catastrophic failure. Riveros et al. (2007) investigated a statistical pattern recognition approach based on measured vibration data, considering both auto-regressive (AR) and auto-regressive with exogeneous inputs (ARX) models. More recently, Huang et al. (2012) investigated the use of an integrated magnetic flux leakage (MFL) and vibration-based monitoring approach, in which a robotic crawler carrying MFL sensors would be deployed to potential damage locations identified through vibration-based monitoring. One of the biggest challenges in developing a robust structural health monitoring approach for deep water risers, as well as other FSI applications, is addressing the considerable uncertainty in FSI response and in fatigue crack propagation. FSI simulation, however, provides a powerful tool for addressing these uncertainties through robust parametric studies, which can both improve fatigue life prediction, and can be used to evaluate and train SHM approaches. To this end, and as an extension to the aforementioned studies, this paper presents a numerical modeling approach for FSI simulation with crack propagation. The modeling approach couples a massively parallel lattice Boltzmann (LB) fluid solver (executed on a graphics processing unit (GPU) device) with an extended finite element (XFE) solid solver. Two-way interaction between the solvers is handled by an immersed boundary (IB) coupling scheme, in which

a Lagrangian solid mesh moves on top of a fixed Eulerian fluid grid. The modeling approach takes advantage of several inherent features of the integrated solvers, namely: (1) scalable GPU parallelization of the LB fluid solver, as well as its ability to handle unsteady turbulent flow with relative ease; (2) the reduced mesh-dependence of the XFE method for modeling crack propagation; and (3) the ability of the IB coupling scheme to handle large-displacement response without global adaptive meshing. The coupled LB-XFE framework developed in this paper offers a versatile and computationally efficient approach for simulating FSI response with crack propagation. Through the development of robust parametric studies, the modeling approach will improve fatigue life prediction for FSI applications, and will aid in the development of SHM approaches for early damage detection by facilitating investigations of damage-sensitive features and sensor arrays.

1.2 ORGANIZATION

The remainder of this thesis is organized as follows:

- Chapters 2, 3, and 4 present the theoretical basis and numerical implementation of the LB fluid solver, the XFE solid solver, and the IB coupling scheme, respectively.
- Chapter 5 presents the benchmark simulations used to validate the modeling approach for FSI and crack propagation simulation.
- Chapter 6 presents an idealized, yet illustrative, demonstration problem for the modeling approach that investigates subcritical crack growth in a flexible beam excited by vortex-induced vibration.

- Chapter 7 provides a comprehensive summary for the study and presents recommendations for future work.

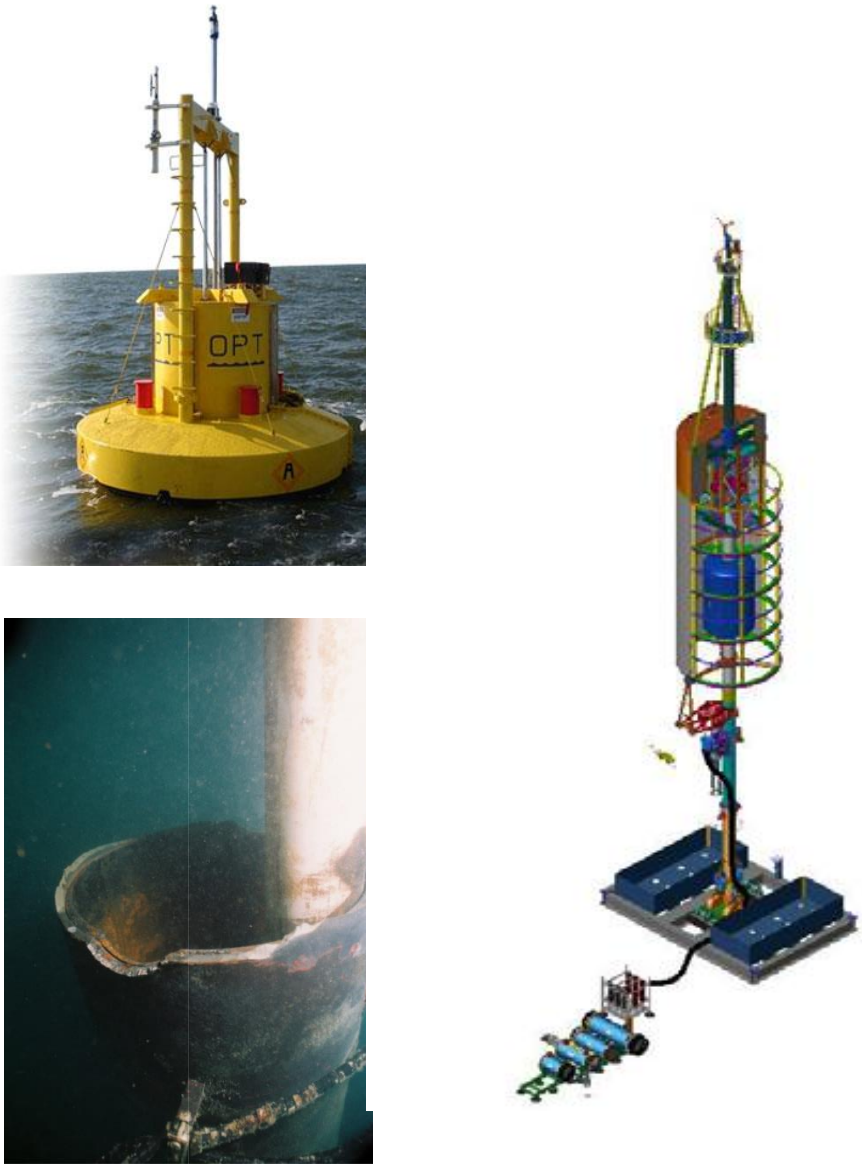

Figure 1.1. Fatigue failure of a power generation buoy
(Photographs and illustration provided by H. Nied)

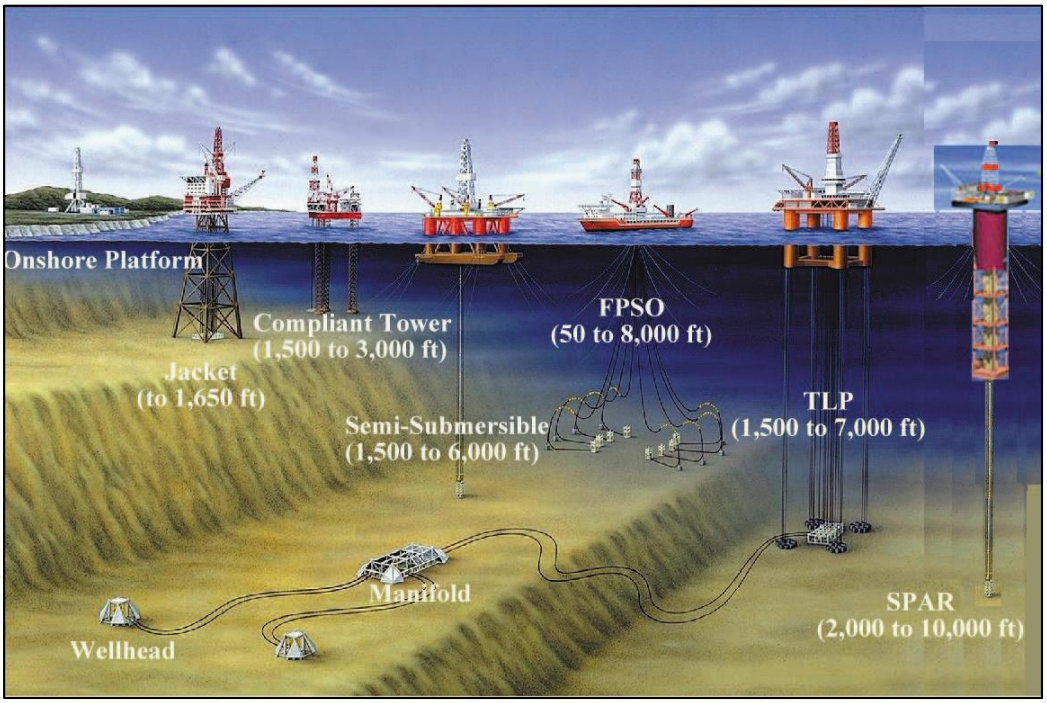

Figure 1.2. Offshore floating production platforms (ACRIGS, 2015)

CHAPTER 2

LATTICE BOLTZMANN FLUID SOLVER

2.1 THEORY AND NUMERICAL IMPLEMENTATION

The lattice Boltzmann (LB) method is a mesoscale modeling approach that simulates fluid dynamics through the transport of fluid particles. Macroscopic physical phenomena, such as the conservation laws described by the Navier-Stokes equations, emerge from the large number of local interactions, considering particle streaming and collision processes. The LB method is generally formulated for a regular fixed point lattice (Eulerian grid), such as the D2Q9 (2-dimension, 9-directional vector) and the D3Q24 (3-dimension, 24-directional vector) lattices shown in Figure 2.1, where the particle streaming directions are governed by the lattice type. The macroscopic fluid dynamics of the system are determined by solving the discrete Boltzmann equation at each node, which in the absence of external forces can be expressed as:

$$\frac{\partial f_\alpha}{\partial t} + e_\alpha \cdot \nabla f_\alpha = \Omega_\alpha \, , \alpha \in \, [0, \dots, q] \, , e_\alpha \in \, \mathbb{R}^d$$

(Equation 2-1)

In Equation 2-1, f_α is the particle velocity distribution function for direction α, e_α is the set of q discrete directional velocities at each node, and Ω_α is a collision operator that is used to relax the particle density at a node to an equilibrium value based on Maxwell-Boltzmann distribution. Instead of numerically integrating the temporal and spatial derivative operators, the LB method handles them discretely in time and space by

streaming particle distributions from a source node to neighboring sites in each direction, as expressed by Equation 2-2.

$$f_\alpha(\boldsymbol{r} + e_\alpha, t+1) - f_\alpha(\boldsymbol{r}, t) = \Omega_\alpha$$

(Equation 2-2)

In Equation 2-2, $\boldsymbol{r}$ is the position vector for a given node and t is the current time in lattice units. Local macroscopic fluid density ρ and velocity $\dot{\boldsymbol{u}}$ are then computed as moments of the particle distribution function f_α using Equations 2-3 and 2-4, respectively.

$$\rho = \sum_{\alpha=0}^{q-1} f_\alpha$$

(Equation 2-3)

$$\dot{\boldsymbol{u}} = \frac{1}{\rho} \sum_{\alpha=0}^{q-1} f_\alpha e_\alpha$$

(Equation 2-4)

Local fluid pressure is then determined according to Equation 2-5 as the product of the local density ρ and the square of the lattice speed of sound c_s.

$$p = \rho c_s^2$$

(Equation 2-5)

For the D2Q9 lattice, the speed of sound is set to $\sqrt{1/3}$, and the discrete velocities $\boldsymbol{e}_\alpha$ are given by Equation 2-6.

$$\boldsymbol{e}_\alpha = \begin{cases} (0,0) & \alpha = 0 \\ \left(cos\left[(\alpha-1)\,{}^{\pi}/_{2}\right], sin\left[(\alpha-1)\,{}^{\pi}/_{2}\right]\right)c_s & \alpha = 1,2,3,4 \\ \left(cos\left[(\alpha-5)\,{}^{\pi}/_{2}+{}^{\pi}/_{4}\right], sin\left[(\alpha-5)\,{}^{\pi}/_{2}+{}^{\pi}/_{4}\right]\right)\sqrt{2}c_s & \alpha = 5,6,7,8 \end{cases}$$

(Equation 2-6)

The LB method is formulated in lattice units, which involves nondimensionalizing the physical system and then converting to the lattice scale. Two input parameters (e.g. spatial and temporal resolution) are specified, leaving the relaxation parameter(s) and viscosity to be calculated accordingly in order to preserve Reynolds number (Re) (i.e. Re is similar in the physical and lattice scales).

2.1.1 Single Relaxation Time Bhatnagar-Gross-Krook (BGK) Scheme

The simplest form of the collision operator is the single relaxation time Bhatnagar-Gross-Krook (BGK) operator (Equation 2-7), which assumes that all kinematic modes relax at the same rate (Bhatnagar et al. 1954).

$$\Omega_\alpha^{BGK} = -\frac{1}{\tau}\left(f_\alpha - f_\alpha^{eq}\right)$$

(Equation 2-7)

In Equation 2-7, τ is a tunable relaxation parameter and f_α^{eq} is the equilibrium particle distribution given by Equation 2-8.

$$f_\alpha^{eq} = \rho w_\alpha \left[1 + \frac{(\boldsymbol{e}_\alpha \cdot \boldsymbol{u})}{c_s^2} + \frac{(\boldsymbol{e}_\alpha \cdot \boldsymbol{u})^2}{c_s^4} - \frac{1}{2}\left(\frac{\boldsymbol{u}\cdot\boldsymbol{u}}{c_s^2}\right)\right]$$

(Equation 2-8)

The weight functions w_α in Equation 2-8 are given by Equation 2-9:

$$w_\alpha = \begin{cases} \frac{4}{9} & \alpha = 0 \\ \frac{1}{9} & \alpha = 1,2,3,4 \\ \frac{1}{36} & \alpha = 5,6,7,8 \end{cases}$$

(Equation 2-9)

The BGK relaxation parameter τ is related to the fluid kinematic viscosity ν through Equation 2-10.

$$\tau = \frac{\nu}{c_s^2} + \frac{1}{2}$$

(Equation 2-10)

2.1.2 Effect of Relaxation on the Stability and Accuracy of the BGK Scheme

The value of the relaxation parameter τ has to be carefully monitored since it impacts both the stability and accuracy of the simulation. The relaxation parameter has to be larger than 0.5 to maintain non-negative viscosity (below this value, the particle distribution has unbounded growth). On the other end of the spectrum, when τ is greater than 1.0, the system is under-relaxed, where the distribution gradually relaxes toward equilibrium. However, in this scenario, accuracy is degraded as τ becomes much larger than 1.0 due to the presence of error terms that are otherwise effectively canceled when τ is less than 1.0. The desired behavior generally occurs when τ is between 0.7 and 1.0. In this region, the system is over-relaxed and the particle distribution oscillates around

equilibrium with decaying amplitude. As τ approaches 0.5, the combined effect of these oscillations along with the inherent noise in the streaming process can lead to unbounded growth of the particle distribution function or to the particle distribution function going to zero, in which case the velocity becomes unbounded.

2.1.3 Multiple Relaxation Time (MRT) Scheme

While easy to implement and computationally efficient, the BGK model suffers from stability problems, and is generally limited to simulations where Re is less than 200. This limitation can be attributed to a fixed Prandtl number of 1.0, as well as a fixed ratio between kinematic and bulk viscosity. In order to resolve these deficiencies, a multiple relaxation time (MRT) collision operator was developed by d'Humieres (1992). In the MRT scheme, the basis of the collision operator is changed, using a transformation matrix $\boldsymbol{M}$, in order to form a diagonal relaxation matrix $\boldsymbol{\Omega^{MRT}}$, which is used to control the different modes (kinematic moments) of the system independently. First, the particle distribution functions $\boldsymbol{f}_\alpha$ are projected to moment space using Equation 2-11.

$$\boldsymbol{m} = \begin{pmatrix} \rho \\ E \\ \varepsilon \\ j_x \\ q_x \\ j_y \\ q_y \\ p_{xx} \\ p_{yy} \end{pmatrix} = \begin{pmatrix} 1 & 1 & 1 & 1 & 1 & 1 & 1 & 1 & 1 \\ -4 & -1 & -1 & -1 & -1 & 2 & 2 & 2 & 2 \\ 4 & -2 & -2 & -2 & -2 & 1 & 1 & 1 & 1 \\ 0 & 1 & 0 & -1 & 0 & 1 & -1 & -1 & 1 \\ 0 & -2 & 0 & 2 & 0 & 1 & -1 & -1 & 1 \\ 0 & 0 & 1 & 0 & -1 & 1 & 1 & -1 & -1 \\ 0 & 0 & -2 & 0 & 2 & 1 & 1 & -1 & -1 \\ 0 & 1 & -1 & 1 & -1 & 0 & 0 & 0 & 0 \\ 0 & 0 & 0 & 0 & 0 & 1 & -1 & 1 & -1 \end{pmatrix} \begin{pmatrix} f_0 \\ f_1 \\ f_2 \\ f_3 \\ f_4 \\ f_5 \\ f_6 \\ f_7 \\ f_8 \end{pmatrix} = \boldsymbol{M} \cdot f_\alpha$$

(Equation 2-11)

In Equation 2-11, the individual modes correspond to density (ρ), energy (E), energy squared (ε), momentum in the X-direction (j_x), energy flux in the X-direction (q_x), momentum in the Y-direction $\left(j_y\right)$, energy flux in the Y-direction $\left(q_y\right)$, the diagonal stress tensor (p_{xx}), and the off-diagonal stress tensor $\left(p_{xy}\right)$, respectively. The collision process is then calculated in moment space using Equation 2-12.

$$f_\alpha(\boldsymbol{r} + e_\alpha, t+1) - f_\alpha(\boldsymbol{r}, t) = \boldsymbol{M}^{-1}\boldsymbol{S}(\boldsymbol{m}(\boldsymbol{r}, t) - \boldsymbol{m}^{\boldsymbol{eq}}(\boldsymbol{r}, t))$$

(Equation 2-12)

In Equation 2-12, $\boldsymbol{S}$ is a diagonal relaxation matrix equal to:

$$\boldsymbol{S} = diag(s_0, s_1, \dots, s_8)$$

(Equation 2-13)

The relaxation rates $s_7 = s_8 = s_\nu$ and $s_1 = s_E$ are related to the kinematic viscosity ν and bulk viscosity ζ, respectively, through Equation 2-14 and Equation 2-15.

$$\nu = c_s^2\left(\frac{1}{s_\nu} - \frac{1}{2}\right)$$

(Equation 2-14)

$$\zeta = c_s^2\left(\frac{1}{s_E} - \frac{1}{2}\right)$$

(Equation 2-15)

Since collisions do not change the conserved quantities (e.g. density and momentum), only the non-conserved moments are updated (i.e. $s_0 = s_3 = s_5 = 0$). Therefore, s_1, s_2, s_4, s_6, s_7, and s_8 are available as tunable parameters.

In Equation 2-12, $\boldsymbol{m}^{\boldsymbol{eq}}(\boldsymbol{r}_i, t)$ is the corresponding equilibrium state in momentum space, given by Equation 2-16.

$$\boldsymbol{m}^{\boldsymbol{eq}}(\boldsymbol{r}_i, t) = \begin{pmatrix} \rho \\ \frac{1}{4}\beta_2\rho + \frac{1}{6}\gamma_2\left(j_x^2 + j_y^2\right) \\ \frac{1}{4}\beta_3\rho + \frac{1}{6}\gamma_4\left(j_x^2 + j_y^2\right) \\ j_x \\ \frac{1}{2}c_1 j_x \\ j_y \\ \frac{1}{2}c_1 j_y \\ \frac{3}{2}\gamma_1\left(j_x^2 - j_y^2\right) \\ \frac{3}{2}\gamma_3\left(j_x j_y\right) \end{pmatrix}$$

(Equation 2-16)

This equilibrium vector introduces seven additional parameters: β_2, β_2, c_1, γ_1, γ_2, γ_3, and γ_4. Galilean invariance of the transverse and sound modes leads to: $\gamma_1 = \gamma_3 = \frac{2}{3}$, and $\gamma_2 = 18$. In addition, isotropy of the attenuation of the transverse mode and Galilean invariance of the attenuation of the sound modes lead to: $c_1 = -2$ and $\beta_2 = -8$. This leaves only two remaining adjustable parameters: β_2 and γ_4. If $\beta_2 = 4$ and $\gamma_4 = -18$,

then $s_1 = s_2 = s_4 = s_6 = s_7 = s_8 = \frac{1}{\tau}$ and the MRT scheme degenerates to the BGK model. The reader is referred to Lallemand and Luo (2000), d'Humieres et al. (2001), Bouzidi et al. (2001), Fakhari and Lee (2013), and Guo et al. (2013) for additional details.

The MRT scheme provides enhanced control over the dissipation of system noise and, as a result, is able to simulate higher Re flows compared with the BGK model. As an illustration, Gorban and Packwood (2014) present stable MRT LB simulations with Re approaching $1x10^5$.

2.1.4 Mach Restriction

In addition to its intrinsic noisy character, the LB method is also plagued by physical properties such as non-Galilean invariance (due to the density dependence of convection) and a non-physical dependence of the pressure on velocity (Succi, 2001). Both of these shortcomings are related to the fact that the LB method is based on perturbative expansion so that it cannot exactly match the Navier-Stokes inertial and pressure tensors. However, for quasi-incompressible low Mach flows (generally less than 0.2) these errors become small and the solution mimics incompressible Navier-Stokes flow.

2.1.5 Boundary Conditions

In the LB method, non-slip, fixed wall boundaries can be modeled as bounce-back conditions, where the particle concentration directed into the wall is reflected back into the fluid domain (Maier et al. 1996), as illustrated in Figure 2.2. Velocity and pressure gradient boundaries can be modeled using the approach developed by Zou and He (1997), which assumes bounceback of the non-equilibrium particle distribution to solve for the

component distributions at the boundary (an otherwise indeterminate problem). Curved or inclined boundaries are handled in the LB method through nodal interpolation.

2.2 IMPLEMENTATION ON GRAPHICS PROCESSING UNIT (GPU) DEVICES

While conceptually straightforward and relatively easy to implement, it is well recognized that the LB method is particularly computationally intensive and memory demanding. Considerations for precision and stability, along with the typical restriction to a regular grid, require that a large number of lattice points are generally needed to discretize a problem domain. In addition, the LB method requires storage of each f_α value throughout the lattice (e.g. 9 values for the D2Q9 lattice or 27 values for the D3Q27 lattice). This storage demand is roughly double the requirement of more traditional finite volume or finite element Navier-Stokes solvers, and also requires greater memory bandwidth for the data to be streamed into the computing cores. In fact, researchers have found that this memory bandwidth requirement is generally what governs the performance of an LB simulation, requiring a large number of CPU cores due to the comparatively limited memory bandwidth that each CPU core has available to it (Blair, 2012).

In order to address the aforementioned computational demands and improve the efficiency of LB simulations, researchers have investigated implementing the LB method on graphics processing unit (GPU) devices (Blair, 2012). These high-throughput devices can run hundreds to thousands of threads (as compared to 16-threads on an 8-core multi-

threaded CPU workstation). For single precision arithmetic, GPU devices can provide a significant boost in the number of floating point operations performed per second, and can outcompete CPU clusters for applications with high memory bandwidth demands, such as LB simulation.

As an illustration of realizable GPU acceleration, Figure 2.3 presents the observed speedup for 2-D channel flow simulations with $4x10^6$ and $18x10^6$ degrees of freedom (DOF), respectively. The serial CPU-based simulations were run on a 3.1 GHz XEON E5-2687 processor (51.2 GB/s memory bandwidth), while the parallel GPU-based simulations were run on an NVIDIA K5000 graphics card (1536 CUDA cores, 173 GB/s memory bandwidth). Performance was measured in terms of lattice updates per second. For the $4x10^6$ and $18x10^6$ DOF models, the observed speed-ups were 19x and 34x, respectively.

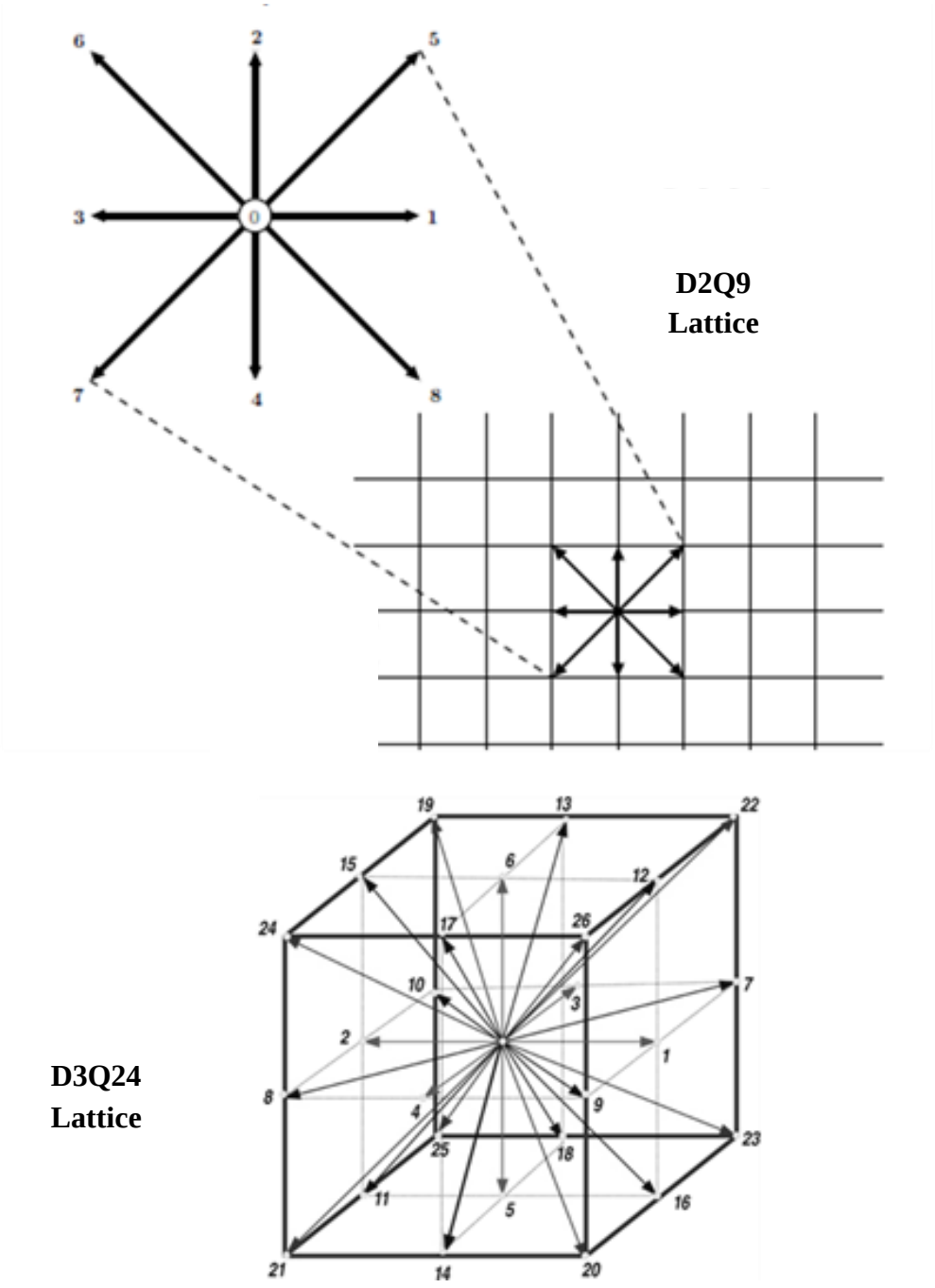

Figure 2.1 D2Q9 and D3Q24 lattices (adapted from Chirila, 2010).

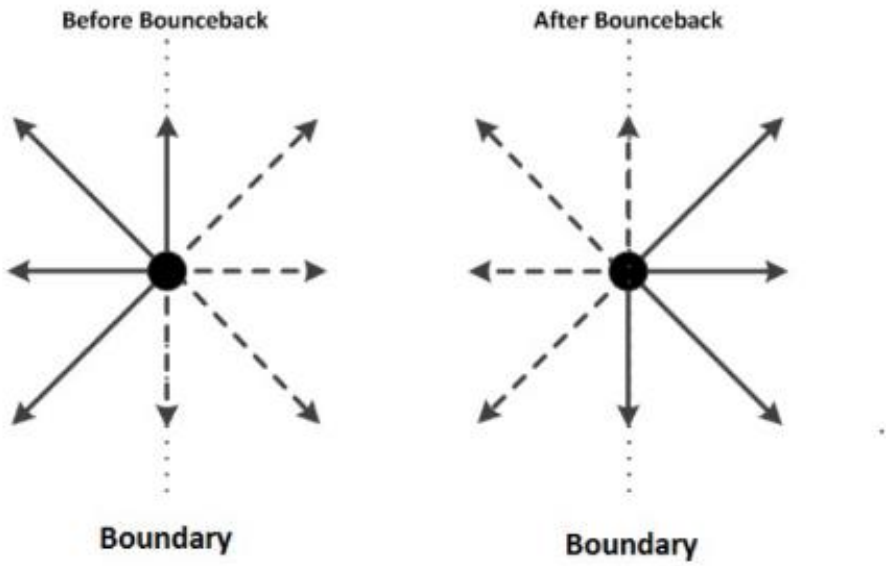

Figure 2.2 Bounceback scheme for non-slip boundaries (Blair, 2012).

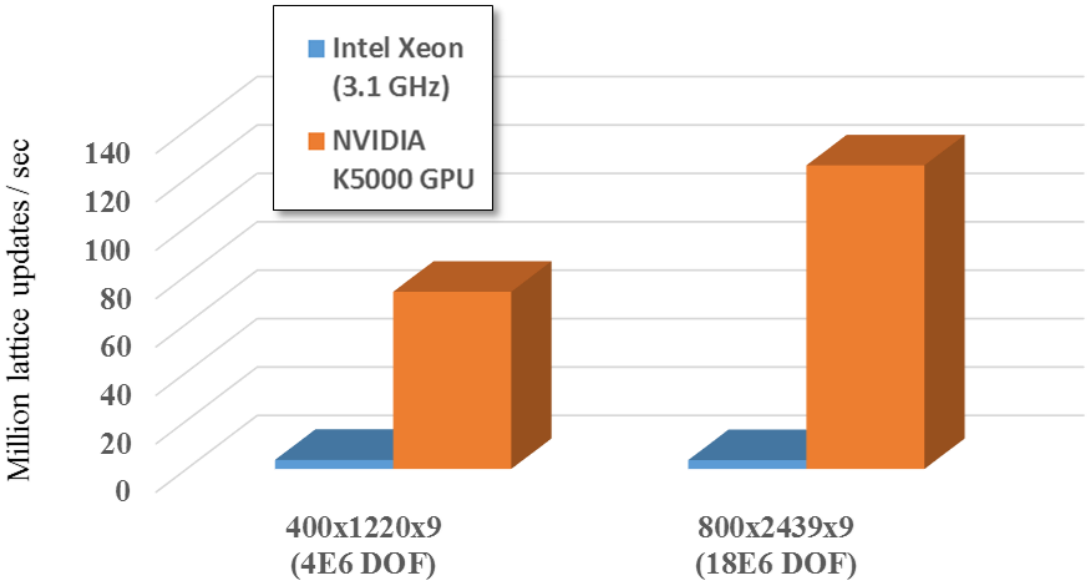

Figure 2.3 Comparison of CPU and GPU performance

CHAPTER 3

EXTENDED FINITE ELEMENT SOLID SOLVER

The extended finite element (XFE) code used in this study extends the XFE code developed by Pais (2011) by accounting for dynamic effects and subcritical crack growth during variable amplitude loading from feedback-driven fluid-structure interaction. An overview of the XFE method is provided in this Chapter. The reader is referred to Belytschko and Black (1999), Karihaloo and Xiao (2003), Sukumar et al. (2005), Bordas et al. (2006), Yazid et al. (2009), Belytschko et al. (2009), and Fries and Belytschko (2010) for additional details.

3.1 EXTENDED FINITE ELEMENT METHOD

3.1.1 Displacement Field Enrichment

The XFE method modifies conventional finite element (FE) analysis by enriching the displacement field to model arbitrarily oriented discontinuities in a traditional FE mesh. In contrast to cohesive zone models that restrict cracking along defined interfaces, the XFE method models discontinuities independent of the mesh by enriching the degrees of freedom (DOF) for the elements cut by the discontinuity. For a simple 2-D plane strain/plane stress element, the displacement field becomes a linear combination of conventional FE DOF and enriched DOF, as shown in Equation 3-1.

$$\boldsymbol{u}^h(x) = \sum_{I\in\Omega} N_I(x)\left[\boldsymbol{u}_I + \sum_{I\in\Omega_d} v(x)\boldsymbol{a}_I\right]$$

(Equation 3-1)

In Equation 3-1, Ω is the analytical domain, Ω_d is the subdomain containing discontinuities, $N_I(x)$ are the traditional finite element shape functions, $v(x)$ is the discontinuous enrichment function, and $\boldsymbol{u}_I$ and $\boldsymbol{a}_I$ are the traditional and enriched DOF, respectively.

3.1.2 Tracking of Discontinuities

Since the discontinuities are not defined by the FE mesh, the level set method (Osher and Sethian, 1988) is used to track their boundaries. For crack modeling, this approach utilizes two tracking functions. The first is based on the Heaviside function and is used for tracking elements completely cut by a crack (Moes et al. 1999).

$$\psi(x) = \begin{cases} +1 & \text{Above Crack} \\ -1 & \text{Below Crack} \end{cases}$$

(Equation 3-2)

The second tracking function is for partially cut elements containing the crack tip, and is formulated in the local crack tip coordinate system in order to more easily track crack tip orientation (Fleming et al. 1997).

$$\phi_a(x) = \left[\sqrt{r}\,sin\frac{\theta}{2}, \sqrt{r}\,cos\frac{\theta}{2}, \sqrt{r}\sin\theta\,cos\frac{\theta}{2}, \sqrt{r}\sin\theta\,sin\frac{\theta}{2},\right]$$

(Equation 3-3)

Illustrations of the signed distance function for a closed domain (inclusion type) and an open section (crack type) are presented in Figure 3.1 The tracking functions are set to zero along the crack surface so that the crack path can be defined at a particular time point by differentiating with respect to time and setting the function to zero.

$$\frac{\partial \phi}{\partial t} + \frac{\partial x(t)}{\partial t} \cdot \frac{\partial \phi}{\partial x(t)} = 0$$

(Equation 3-4)

Figure 3.2 illustrates how a discontinuity (e.g. an edge crack) can be accommodated by enrichment of the displacement field, and how the level set functions are used to track the boundaries of the discontinuity (e.g. the crack path).

It is noted that in the XFE method, the integrands for numerical integration can contain a discontinuity, which presents problems for a conventional Gauss quadrature rule. One solution is to use Delaunay triangulation to subdivide the enriched elements into triangular regions between the crack and element boundaries (Mohammadi, 2008). The process is illustrated in Figure 3.3 for an element completely cut by a crack and an element containing a crack tip. Separate integration points and weights are the used for each triangular element, and the final integral is calculated as the summation over all of the Gauss points in the original element.

3.2 CRACK GROWTH MODEL

3.2.1 Angle of Divergence and Growth Rate

Crack growth in the XFE solver is based on the maximum circumferential tensile stress criterion (Sih, 1974), where crack extension occurs in the direction of maximum circumferential stress. The divergence angle of crack growth, relative to the current orientation of the crack tip, is then given by Equation 3-4 (Moes et al. 1999).

$$\theta_c = 2\arctan\frac{1}{4}\left[\frac{K_I}{K_{II}} - \underline{+}(K_{II})\sqrt{\left(\frac{K_I}{K_{II}}\right)^2 + 8}\right]$$

(Equation 3-4)

In Equation 3-4, K_I and K_{II} are the mode I (crack opening) and mode II (crack sliding) stress intensity factors (SIF), respectively, where the crack deformation modes are illustrated in Figure 3.4.

In fatigue load simulations, accurate modeling of mixed-mode crack growth would require extensive experimental data that considers all possible load configurations and load histories. However, a practical (albeit idealized) simplification can be made by assuming mode I dominance and basing crack extension on experimentally measured mode I behavior. Under the assumption of small scale yielding at the crack tip (i.e. linear elastic fracture mechanics (LEFM)), a relationship can then be established between the crack growth increment $\left(\frac{da}{dN}\right)$ and the change in the mode I SIF (ΔK_I). The form of this relationship for a particular application is derived by fitting experimental data, and should

consider all applicable conditions that impact crack extension (e.g. stress range, loading rate, overload occurrence, crack closure, and crack surface loading). Since the objective of the current study is to integrate a general crack modeling approach into an FSI framework, the simple two-parameter power law model developed by Paris et al. (1961) is used in the present study:

$$\frac{da}{dN} = C(\Delta K_I)^n \quad \text{if} \quad \Delta K_I > \Delta K_{th}$$

(Equation 3-5)

In Equation 3-5, C and n are empirical constants used to fit the experimental data. Crack extension occurs when ΔK_I is larger than an experimentally obtained threshold (ΔK_{th}), which is typically an order of magnitude smaller than the fracture toughness of the material (K_{IC}).

3.2.2 J-Integral

The SIF utilized in Equation 3-4 and 3-5 are determined in a FE simulation using a path-independent contour integration referred to as the J-integral (Rice, 1968). The linear elastic fracture mechanics (LEFM) formulation of the J-integral is defined in Equation 3-6 as the relationship between the strain energy near the crack tip and the external work done by tractions acting through the displacement field.

$$J = \int_{\Gamma} \left[W dy - \boldsymbol{t} \frac{\partial \boldsymbol{d}}{\partial x} \right] ds$$

(Equation 3-6)

In Equation 3-6, the strain energy density (W) and external work $\left(\boldsymbol{t}\frac{\partial \boldsymbol{d}}{\partial x}\right)$ are given by Equations 3-7 and 3-8, respectively.

$$W = \frac{1}{2}\left[\sigma_x \frac{\partial u}{\partial x} + \tau_{xy}\left(\frac{\partial u}{\partial y} + \frac{\partial v}{\partial x}\right)\frac{\partial u}{\partial x} + \sigma_y \frac{\partial v}{\partial y}\right]$$

(Equation 3-7)

$$\boldsymbol{t}\frac{\partial \boldsymbol{d}}{\partial x} = \left[\left(\sigma_x n_1 + \tau_{xy} n_2\right)\frac{\partial u}{\partial x} + \left(\tau_{xy} n_1 + \sigma_y n_2\right)\frac{\partial u}{\partial x}\right]$$

(Equation 3-8)

In Equations 3-7 and 3-8, σ_x, σ_y, and τ_{xy} are the stress components; $\frac{\partial u}{\partial x}$, $\frac{\partial v}{\partial y}$, $\frac{\partial u}{\partial y} + \frac{\partial v}{\partial x}$ are the strain components; and n_1 and n_2 are the surface normals; where all terms are in Cartesian coordinates.

The path independence of the J-integral comes from Cauchy's Theorem and the assumption of traction-free boundary conditions along the crack surface. As an illustration, Figure 3.5 shows a closed contour drawn around the tip of a crack, which is formed by two line integrals (C+ and C- along the crack path) and two contours C and Γ. By Cauchy's Theorem, the integration along the closed contour is zero if no singularities are present in the domain. Under the assumption of traction-free boundaries along the crack surface, the line integral contributions are zero because the integration is along the local x-direction (i.e. both terms in Equation 3-6 are zero). The resulting equation states that the integration along contour C plus contour gamma is zero, or, equivalently, that the two integrals are

equal. This path independence enables consistent calculation of the J-integral from FE results for any reasonably prescribed J-integral search radius (Figure 3-6).

It is noted that the assumption of traction-free boundaries at the crack surface is clearly violated in FSI applications where the crack surface is loaded by hydraulic pressure. However, if the strain demand from the crack surface loading is small relative to the integrated effect of the structural surface tractions and body forces, the assumption of a traction-free crack surface may still be appropriate. For simplicity, the simulations in this thesis neglect hydraulic loading of the crack surface.

3.2.3 Interaction Integral Method

The separation of mode I and mode II SIFs, is accomplished through the interaction integral method (Nikishkov and Atlui, 1987). In this approach, auxiliary stress fields (considering pure mode response) are superimposed on top of the real stress fields. For this study, the auxiliary stress and displacement equations developed by Westergaard (1939) and Williams (1957) are utilized. This choice results in the superposition of separate J-integral terms for the real and auxiliary stress fields as well as an interaction integral (I) for the actual stresses acting through the auxiliary strain field, integrated over the element area (A).

$$I^{(Mode\ I,\ \ Mode\ II)} = \int_{\mathrm{A}} \left[\sigma_{ij}^{(1)} \frac{du_i^{(2)}}{dx_1} - \sigma_{ij}^{(1)} \frac{du_i^{(1)}}{dx_1} - W^{(1,2)} \delta_{1j} \right] \frac{\partial q}{\partial x_j} d\mathrm{A}$$

(Equation 3-9)

In Equation 3-9, superscripts 1 and 2 denote the real and auxiliary fields, respectively; and δ_{1j} is the Dirac delta function. Since we can also relate the modal SIFs to the stress/strain fields, Equation 3-9 establishes a relationship between the interaction integral and the SIFs. By advantageously choosing pure mode response for the auxiliary fields, we can then separate the mode I and mode II SIFs using Equation 3-10 and 3-11.

$$K_I = \frac{I^{(Mode\ I)} E_{eff}}{2}$$

(Equation 3-10)

$$K_{II} = \frac{I^{(Mode\ II)} E_{eff}}{2}$$

(Equation 3-11)

In Equation 3-10 and 3-11, E_{eff} is the effective elastic modulus, equal to E for plane stress or $\frac{E}{1-\nu^2}$ for plane strain.

3.3 DYNAMIC SOLID SOLVER

3.3.1 Equations of Motion

The dynamic equations of motion for the solid solver are given by:

$$\boldsymbol{M\ddot{u} + C\dot{u} + Ku = F}$$

(Equation 3-12)

In Equation 3-12, $\boldsymbol{M}$, $\boldsymbol{C}$, and $\boldsymbol{K}$ are the global mass, damping, and stiffness matrices, respectively. The global force vector is denoted as $\boldsymbol{F}$. The property matrices utilized in the

equations of motion include both conventional and XFE terms, as illustrated in Equation 3-13 for the tangent stiffness matrix ($\boldsymbol{K}^T$).

$$\boldsymbol{K}^T = \begin{bmatrix} \boldsymbol{K^{cc}} & \boldsymbol{K^{cx}} \\ \boldsymbol{K^{xc}} & \boldsymbol{K^{xx}} \end{bmatrix}$$

(Equation 3-13)

In Equation 3-13, c and x denote conventional and enriched DOF, respectively. The mass matrix is expanded in a similar fashion using the approach developed by Menouillard (2006) to activate and deactivate inertial DOF.

$$\boldsymbol{M^e}_{\boldsymbol{n}} = \frac{M_o}{N_n} \int_{\Omega} {\psi_i}^2 d\Omega$$

(Equation 3-14)

In Equation 3-14, $\boldsymbol{M^e}_{\boldsymbol{n}}$ is the lumped mass at node $\boldsymbol{n}$ in element $\boldsymbol{e}$, M_o is the element mass, N_n is the number of nodes in the element, ψ is the previously defined tracking function, and Ω is the element domain. Crack closure is modeled by reverting to the initial stiffness matrix when a set of predefined contact conditions are met, which involves monitoring both crack opening amplitude and direction.

3.3.2 Damping

In order to reduce artificial high frequency excitation stemming from numerical noise in the lattice Boltzmann (LB) fluid solver (discussed in Chapter 4), Rayleigh mass and

stiffness proportional damping was utilized with target modal damping ratios of 1% of critical in the first and second modes of vibration.

$$\boldsymbol{C} = a_o \boldsymbol{M} + a_1 \boldsymbol{K} \quad \text{(Equation 3-15)}$$

In Equation 3-15, a_o and a_1 are the mass and stiffness proportionality coefficients, respectively. It is noted, however, that Rayleigh damping is a computationally expensive approach to controlling system noise since the proportionality coefficients need to be updated at each nonlinear event in order to preserve the target modal damping ratios. With this in mind, future development of the code will likely move to an integration scheme like the Hilber-Hughes-Tayler (HHT) model (Hilber et al. 1977), which provides numerical damping in the higher modes, while keeping damping in the fundamental modes at a minimum. This minimization can be important for movement-induced excitation (MIE) scenarios where the response is sensitive to damping in the fundamental modes. In addition, and as will be discussed in Chapter 4, running the fluid and solid solver at different time scales and averaging hydraulic pressures has been shown to significantly reduce this artificial high frequency excitation.

3.3.3 Nonlinear Newmark Average Acceleration Method

Solution of the system of equations is accomplished using the implicit nonlinear Newmark average acceleration method (Chopra, 2007). A summary of the procedure is outlined below.

Initial calculations…

- Set the initial acceleration of the system $\ddot{\boldsymbol{u}}_{\boldsymbol{0}}$

$$\ddot{\boldsymbol{u}}_{\boldsymbol{0}} = (\boldsymbol{F}_0 - \boldsymbol{C}\dot{\boldsymbol{u}}_{\boldsymbol{0}} - (\boldsymbol{f}_{\boldsymbol{s}})_{\boldsymbol{0}})/\boldsymbol{M}$$

(Equation 3-16)

In Equation 3-16, $\boldsymbol{F}_0$ and $\dot{\boldsymbol{u}}_{\boldsymbol{0}}$ are the initial values of external force and nodal velocity, respectively, and $(\boldsymbol{f}_{\boldsymbol{s}})_{\boldsymbol{0}}$ is the initial force due to imposed displacement.

- Select time step Δt

- Calculate constants of integration $\boldsymbol{a}$ and $\boldsymbol{b}$

$$\boldsymbol{a} = \frac{1}{\beta \Delta t}\boldsymbol{M} + \frac{\gamma}{\beta}\boldsymbol{C} \qquad \boldsymbol{b} = \frac{1}{2\beta}\boldsymbol{M} + \Delta t\left(\frac{\gamma}{2\beta} - 1\right)\boldsymbol{C}$$

(Equation 3-17)

In Equation 3-17, γ and β are integration constants taken as 1/2 and 1/4, respectively, for the Newmark average acceleration method.

Calculations for earch time step i…

- Calculate the effective change in the forcing function $\Delta\widehat{\boldsymbol{F}}_{\boldsymbol{i}}$

$$\Delta\widehat{\boldsymbol{F}}_{\boldsymbol{i}} = \Delta\boldsymbol{F}_{\boldsymbol{i}} + \boldsymbol{a}\dot{\boldsymbol{u}}_{\boldsymbol{i}} + \boldsymbol{b}\ddot{\boldsymbol{u}}_{\boldsymbol{i}}$$

(Equation 3-18)

- Determine the tangent property matrices $\boldsymbol{K_i}$, $\boldsymbol{M_i}$, $\boldsymbol{C_i}$

- Calculate the effective stiffness matrix $\widehat{\boldsymbol{K}}_{\boldsymbol{i}}$

$$\widehat{\boldsymbol{K}}_{\boldsymbol{i}} = \boldsymbol{K_i} + \left(\frac{\gamma}{\beta\ \Delta t}\right)\boldsymbol{C_i} + \left(\frac{1}{\beta(\Delta t)^2}\right)\boldsymbol{M_i}$$

(Equation 3-19)

- Solve for the incremental nodal displacements $\boldsymbol{\Delta u_i}$ from…

$$\boldsymbol{\Delta}\widehat{\boldsymbol{F}}_{\boldsymbol{i}} = \widehat{\boldsymbol{K}}_{\boldsymbol{i}}\,\boldsymbol{\Delta u_i}$$

(Equation 3-20)

- Solve for the incremental nodal velocities and accelerations $\boldsymbol{\Delta \dot{u}_i}$ and $\boldsymbol{\Delta \ddot{u}_i}$

$$\boldsymbol{\Delta \dot{u}_i} = \left(\frac{\gamma}{\beta\ \Delta t}\right)\boldsymbol{\Delta u_i} - \frac{\gamma}{\beta}\boldsymbol{\dot{u}_i} + \Delta t\left(1 - \frac{\gamma}{2\beta}\right)\ddot{u}_i$$

(Equation 3-21)

$$\boldsymbol{\Delta \ddot{u}_i} = \left(\frac{1}{\beta(\Delta t)^2}\right)\boldsymbol{\Delta u_i} - \frac{1}{\beta\ \Delta t}\boldsymbol{\Delta \dot{u}_i} - \frac{1}{2\beta}\boldsymbol{\ddot{u}}_i$$

(Equation 3-22)

- Solve for the instantaneous nodal displacements, velocities, and accelerations

$$\boldsymbol{u_{i+1}} = \boldsymbol{u_i} + \boldsymbol{\Delta u_i}$$

(Equation 3-23)

$$\dot{\boldsymbol{u}}_{\boldsymbol{i+1}} = \dot{\boldsymbol{u}}_{\boldsymbol{i}} + \boldsymbol{\Delta}\dot{\boldsymbol{u}}_{\boldsymbol{i}}$$

(Equation 3-24)

$$\ddot{\boldsymbol{u}}_{\boldsymbol{i+1}} = \ddot{\boldsymbol{u}}_{\boldsymbol{i}} + \boldsymbol{\Delta}\ddot{\boldsymbol{u}}_{\boldsymbol{i}}$$

(Equation 3-25)

Repeat for next time step…

3.4 ADDITIONAL CONSIDERATIONS FOR FATIGUE CRACK MODELING IN FSI APPLICATIONS

There are a number of issues related to modeling fatigue crack growth, particularly for the target FSI application. The first is that the previous derivation of the J-integral assumes monotonic and proportional loading, both of which are violated in cyclic load fatigue cracking scenarios. The previously discussed approach can provide useful information, however, if these conditions are not violated that severely. However, this is a rather subjective statement and, as a result, it clear that experimental data is critical to establishing a relationship between the change in the J-integral and crack growth rate. The combination of SIFs for mixed mode behavior is also problematic when the crack path is curved since the theoretical basis of these factors assumes self-similar or straight line crack advance. As before, if this condition is not violated that severely, the previously described combination may still be appropriate.

Other issues that complicate fatigue crack modeling in FSI applications include crack closure and pressure loading of the crack surface (both of which impact stress conditions

at the crack tip), as well as variable loading in highly turbulent conditions and dynamic response, which make it difficult to develop robust empirical fatigue growth models. The crack growth model, therefore, is only as good as the experimental data used to calibrate it. With this in mind, the goal of the present study was to integrate a general crack modeling approach in FSI simulation, one which could be readily adaptable to more sophisticated experimentally driven growth models.

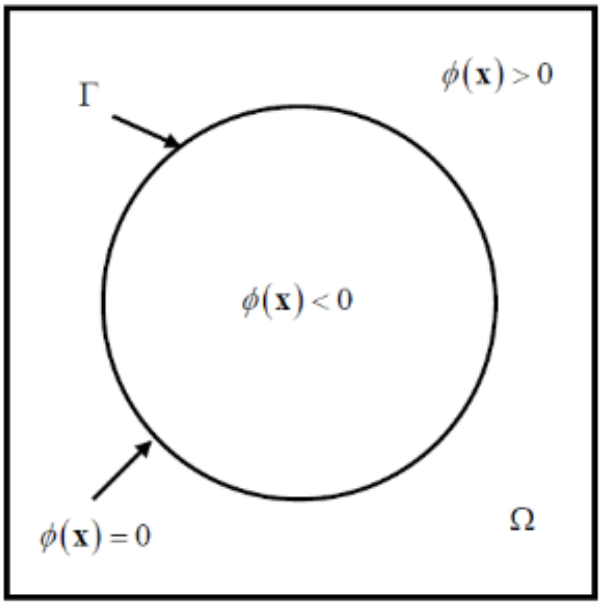

(a)

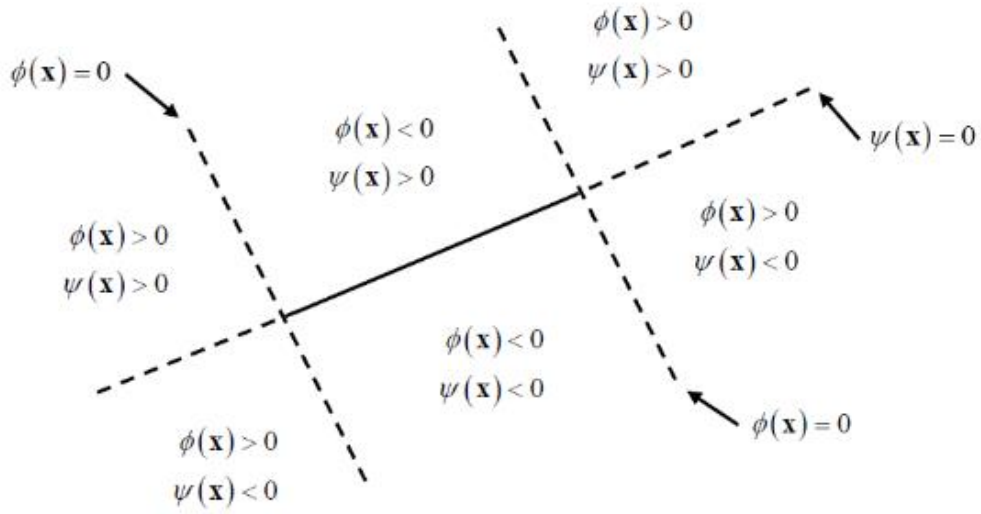

(b)

Figure 3.1 Illustration of the signed distance function for (a) a closed domain and (b) an open section (Pais, 2011)

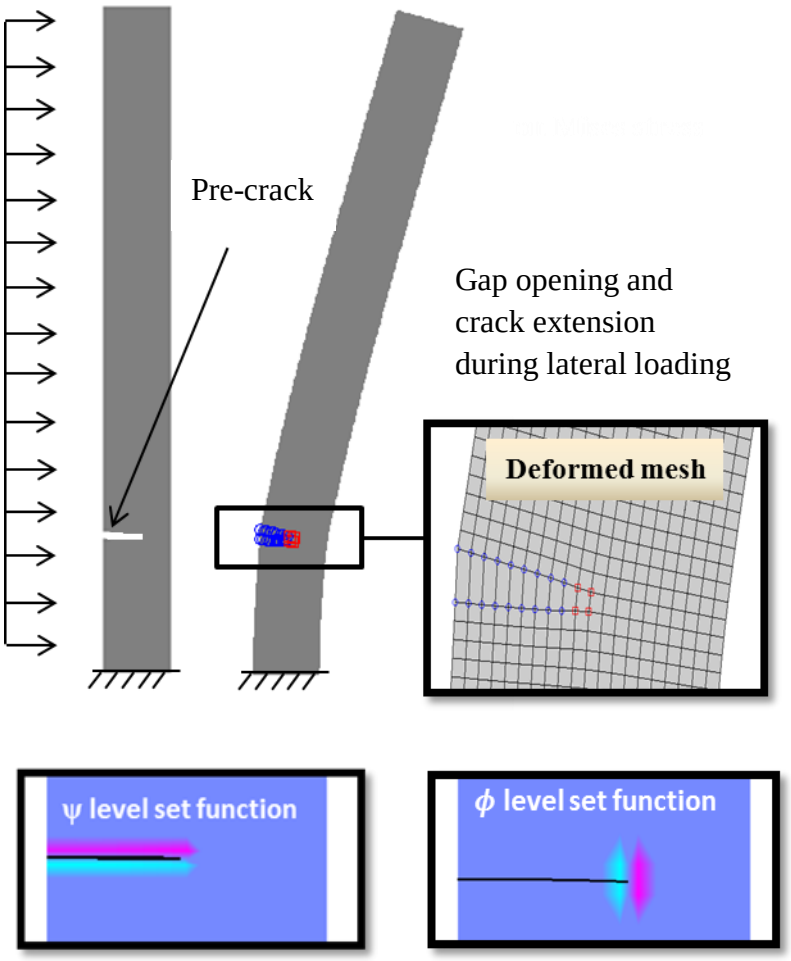

Figure 3.2 Gap opening and crack extension in a pre-cracked beam during lateral load response

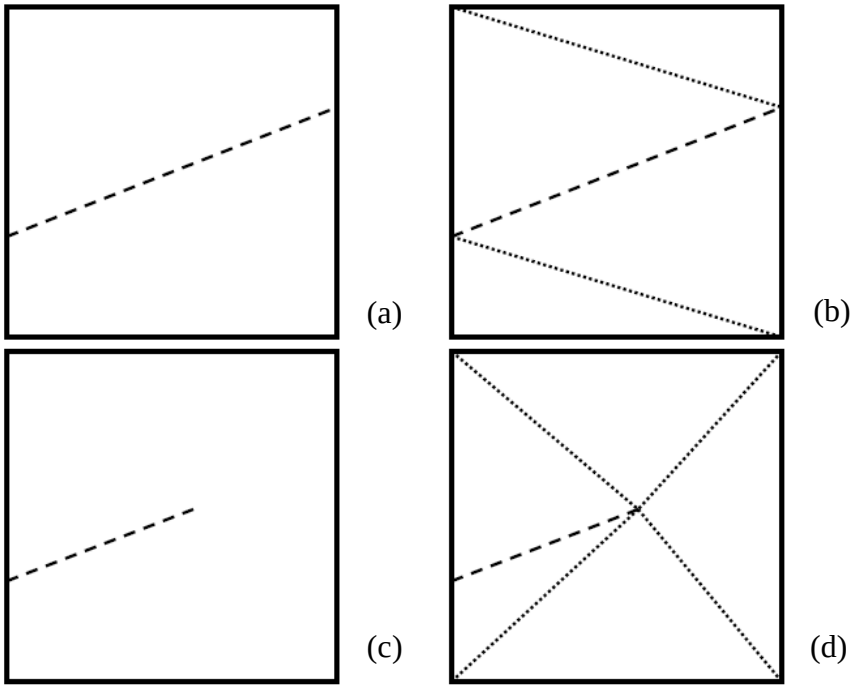

Figure 3.3 Elements containing a discontinuity and the continuous subdomains for integration: (a) element completely cut by the crack, (b) element completely cut by the crack divided into four continous subdomains, (c) element containing the crack tip, and (d) element containing the crack tip divided into five continuous subdomains (Pais, 2011)

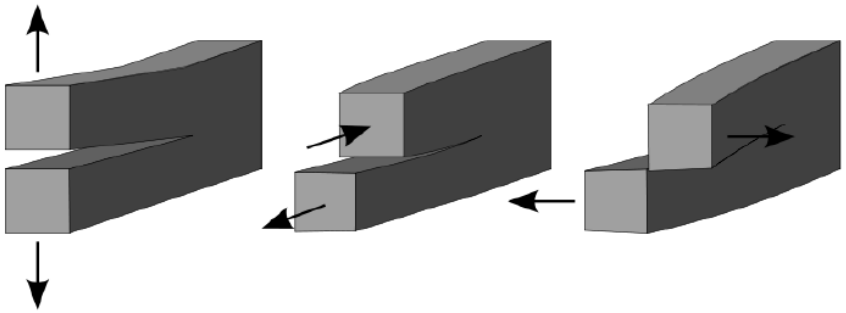

Figure 3.4 Crack deformation modes: mode I (opening), (b) mode II (sliding), and (c) mode III (tearing) (Sanford, 2003)

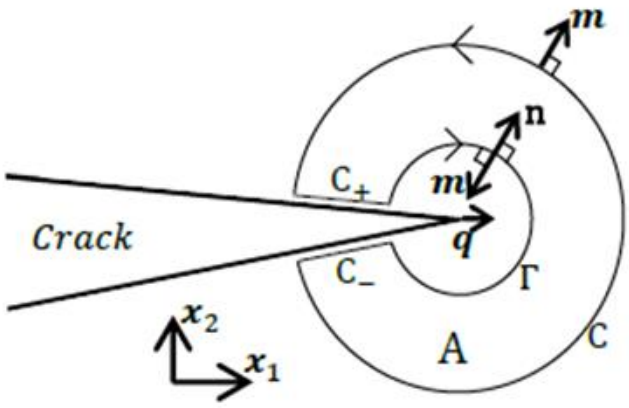

Figure 3.5 Contour integration at the crack tip (Sanford, 2003)

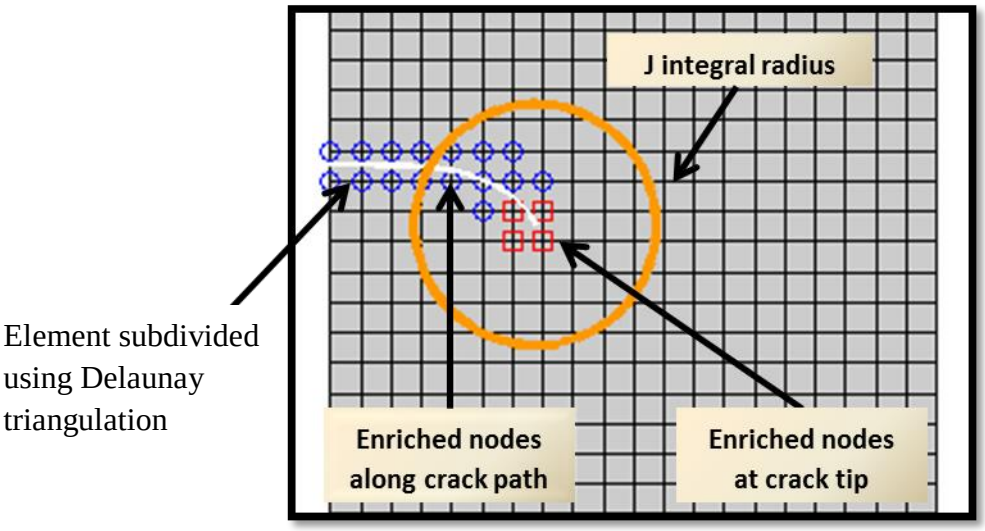

Figure 3.6 J-integral search radius

CHAPTER 4

FLUID-STRUCTURE COUPLING

4.1 GENERAL FRAMEWORK

Coupling of the fluid and solid solvers is accomplished using a variation of the immersed boundary (IB) method (Peskin, 2002), in which a deformable (Lagrangian) solid mesh moves on top of a fixed (Eulerian) fluid lattice. A flowchart for the proposed modeling process is presented in Figure 4.1. After model generation and initialization, hydraulic stresses are calculated at the fluid-structure boundaries. These stress demands, along with inertial forces and strain histories, are used to determine crack growth/closure and the instantaneous material properties for the system. These properties are then fed to the dynamic solid solver, which calculates the incremental change in structural displacement, velocity, and acceleration. The structural velocities are transferred back into the fluid by enforcing continuity along the fluid-structure boundaries. The flow field is then updated to calculate hydraulic pressure at the next time step.

The two-way coupling scheme is summarized by Equations 4-1 and 4-2.

$$p_{fluid}(\boldsymbol{x}, t) \rightarrow p_{solid}(\boldsymbol{x}, t)$$

(Equation 4-1)

$$\dot{u}_{solid}(\boldsymbol{x}, t) \rightarrow \dot{u}_{fluid}(\boldsymbol{x}, t)$$

(Equation 4-2)

Fluid pressures drive structural response and, in turn, the structural velocities are transferred back into the fluid by enforcing velocity continuity along the shared interfaces. This coupling approach is able to handle very stiff to very soft structures, as shown in Figure 4.2 for the case of a flexible beam in steady channel flow. The beam is attached to a rigid circular obstruction and is excited by vortex shedding. Figure 4.2(a) and (b) respectively, show the vibratory response when the beam is relatively stiff (higher elastic modulus), where vibration is dominated by the fundamental mode, and when the beam is relatively flexible (lower elastic modulus), where vibration includes higher modes of response. It is noted that the depiction of the latter case (Figure 4.2(b)) is during the passage of an initial shock wave front that is triggered during initialization of the LB fluid solver.

4.2 BOUNDARY INTERPOLATION FUNCTIONS

Boundary information is exchanged between the two domains by interpolating information from the neighboring nodes, as illustrated in Figure 4.3. It is noted that the choice of distribution functions for information exchange should be evaluated against benchmark data, as it can impact both the stability and accuracy of the simulation. For the present study, the distribution functions presented in Lai and Peskin (2000) are utilized.

4.3 HYDRAULIC PRESSURE

Stresses exerted by the fluid on the solid boundaries are calculated within the fluid solver and are transferred to the solid solver as external forces integrated along the solid boundaries (He and Doolen, 1997):

$$\boldsymbol{F} = \int \boldsymbol{n} \cdot [p\boldsymbol{I} + \rho\upsilon(\nabla\dot{\boldsymbol{u}} + (\nabla\dot{\boldsymbol{u}})^T)]\, dA = \sum_{\alpha=1}^{4} e_\alpha \cdot \left[p\boldsymbol{I} + \tau_{ij}\right] \delta_x$$

(Equation 4-3)

In Equation 4-3, $\boldsymbol{F}$ are the resultant structural forces from hydraulic loading, $\boldsymbol{n}$ is the outward surface normal, $\boldsymbol{I}$ is the identity matrix, and δ_x is the Dirac delta function. The skin friction component (τ_{ij}) is based on the deviatoric stress, which requires spatial partial derivatives that can interfere with the locality of the LB method. An approach has been developed by Kruger et al. (2009) to approximate the deviatoric stress, while still preserving locality, using the non-equilibrium portion of the particle density. In this approach, the shear stress is calculated according to Equation 4-4.

$$\tau_{ij} = \left(1 - \frac{1}{2\tau}\right) \sum_{\alpha=1}^{8} \left[f_\alpha(\boldsymbol{x}, t) - f_\alpha^{eq}(\boldsymbol{x}, t)\right] \times \left(e_{\alpha i} \cdot e_{\alpha j} - \frac{1}{2} e_\alpha \cdot e_\alpha \delta_{ij}\right)$$

(Equation 4-4)

Combining the instantaneous hydraulic forces from Equation 4-3 with the inertial forces, the dynamic solid solver then calculates the dynamic response of the structure.

4.4 ENFORCEMENT OF VELOCITY CONTINUITY

Velocity continuity at the fluid-solid interface is subsequently enforced by modifying the particle distribution at the neighboring fluid nodes using the approach developed by Kwon (2006), as illustrated in Equation 4-5.

$$f_2 \leftarrow f_2 + \frac{\dot{u}_x}{3} \quad f_3 \leftarrow f_3 + \frac{\dot{u}_y}{3} \quad f_4 \leftarrow f_4 - \frac{\dot{u}_x}{3} \quad f_5 \leftarrow f_5 - \frac{\dot{u}_y}{3}$$

$$f_6 \leftarrow f_6 + \frac{\dot{u}_x}{12} + \frac{\dot{u}_y}{12} \quad f_7 \leftarrow f_7 - \frac{\dot{u}_x}{12} + \frac{\dot{u}_y}{12} \quad f_8 \leftarrow f_8 - \frac{\dot{u}_x}{12} - \frac{\dot{u}_y}{12} \quad f_9 \leftarrow f_9 + \frac{\dot{u}_x}{12} - \frac{\dot{u}_y}{12}$$

(Equation 4-5)

4.5 SUBCYCLING OF THE FLUID SOLVER

An important note regarding the coupling scheme is that the inherent high-frequency fluctuations in the LB fluid solver can artificially excite higher mode structural vibrations, as illustrated in Figure 4.4. These artificial high-frequency vibrations can degrade the accuracy of the simulation and can lead to instability. Time averaging of the fluid pressure has been shown to significantly reduce the effect of this artificial noise. This approach is particularly effective and efficient when the minimum time step required for the dynamic solid solver is significantly larger than the time step required for the LB fluid solver. The simulations developed for this study, for example, utilize a solid model where the time step required to capture the vibration modes of interest is an order of magnitude larger than the lattice time step. As a result, running the fluid and solid solvers on different time scales

(e,g. running the fluid solver at every lattice time step and the solid solver at every tenth lattice time step), and using a time-averaged pressure loading has two distinct advantages: (1) reduction of high-frequency noise in the fluid solver and the resulting high-frequency structural excitation, and (2) computational efficiency since the solid solver is only executed at a frequency required to capture the modes of interest. The effect of this time-averaging approach, however, should be investigated against benchmark data to ensure an accurate and stable solution.

CHAPTER 4

FLUID-STRUCTURE COUPLING

4.1 GENERAL FRAMEWORK

Coupling of the fluid and solid solvers is accomplished using a variation of the immersed boundary (IB) method (Peskin, 2002), in which a deformable (Lagrangian) solid mesh moves on top of a fixed (Eulerian) fluid lattice. A flowchart for the proposed modeling process is presented in Figure 4.1. After model generation and initialization, hydraulic stresses are calculated at the fluid-structure boundaries. These stress demands, along with inertial forces and strain histories, are used to determine crack growth/closure and the instantaneous material properties for the system. These properties are then fed to the dynamic solid solver, which calculates the incremental change in structural displacement, velocity, and acceleration. The structural velocities are transferred back into the fluid by enforcing continuity along the fluid-structure boundaries. The flow field is then updated to calculate hydraulic pressure at the next time step.

The two-way coupling scheme is summarized by Equations 4-1 and 4-2.

$$p_{fluid}(\boldsymbol{x}, t) \rightarrow p_{solid}(\boldsymbol{x}, t)$$

(Equation 4-1)

$$\dot{u}_{solid}(\boldsymbol{x}, t) \rightarrow \dot{u}_{fluid}(\boldsymbol{x}, t)$$

(Equation 4-2)

Fluid pressures drive structural response and, in turn, the structural velocities are transferred back into the fluid by enforcing velocity continuity along the shared interfaces. This coupling approach is able to handle very stiff to very soft structures, as shown in Figure 4.2 for the case of a flexible beam in steady channel flow. The beam is attached to a rigid circular obstruction and is excited by vortex shedding. Figure 4.2(a) and (b) respectively, show the vibratory response when the beam is relatively stiff (higher elastic modulus), where vibration is dominated by the fundamental mode, and when the beam is relatively flexible (lower elastic modulus), where vibration includes higher modes of response.

4.2 BOUNDARY INTERPOLATION FUNCTIONS

Boundary information is exchanged between the two domains by interpolating information from the neighboring nodes, as illustrated in Figure 4.3. It is noted that the choice of distribution functions for information exchange should be evaluated against benchmark data, as it can impact both the stability and accuracy of the simulation. For the present study, the distribution functions presented in Lai and Peskin (2000) are utilized.

4.3 HYDRAULIC PRESSURE

Stresses exerted by the fluid on the solid boundaries are calculated within the fluid solver and are transferred to the solid solver as external forces integrated along the solid boundaries (He and Doolen, 1997):

$$\boldsymbol{F} = \int \boldsymbol{n} \cdot [p\boldsymbol{I} + \rho\upsilon(\nabla\dot{\boldsymbol{u}} + (\nabla\dot{\boldsymbol{u}})^T)]\, dA = \sum_{\alpha=1}^{4} e_\alpha \cdot \left[p\boldsymbol{I} + \tau_{ij}\right] \delta_x$$

(Equation 4-3)

In Equation 4-3, $\boldsymbol{F}$ are the resultant structural forces from hydraulic loading, $\boldsymbol{n}$ is the outward surface normal, $\boldsymbol{I}$ is the identity matrix, and δ_x is the Dirac delta function. The skin friction component (τ_{ij}) is based on the deviatoric stress, which requires spatial partial derivatives that can interfere with the locality of the LB method. An approach has been developed by Kruger et al. (2009) to approximate the deviatoric stress, while still preserving locality, using the non-equilibrium portion of the particle density. In this approach, the shear stress is calculated according to Equation 4-4.

$$\tau_{ij} = \left(1 - \frac{1}{2\tau}\right) \sum_{\alpha=1}^{8} \left[f_\alpha(\boldsymbol{x}, t) - f_\alpha^{eq}(\boldsymbol{x}, t)\right] \times \left(e_{\alpha i} \cdot e_{\alpha j} - \frac{1}{2} e_\alpha \cdot e_\alpha \delta_{ij}\right)$$

(Equation 4-4)

Combining the instantaneous hydraulic forces from Equation 4-3 with the inertial forces, the dynamic solid solver then calculates the dynamic response of the structure.

4.4 ENFORCEMENT OF VELOCITY CONTINUITY

Velocity continuity at the fluid-solid interface is subsequently enforced by modifying the particle distribution at the neighboring fluid nodes using the approach developed by Kwon (2006), as illustrated in Equation 4-5.

$$f_2 \leftarrow f_2 + \frac{\dot{u}_x}{3} \quad f_3 \leftarrow f_3 + \frac{\dot{u}_y}{3} \quad f_4 \leftarrow f_4 - \frac{\dot{u}_x}{3} \quad f_5 \leftarrow f_5 - \frac{\dot{u}_y}{3}$$

$$f_6 \leftarrow f_6 + \frac{\dot{u}_x}{12} + \frac{\dot{u}_y}{12} \quad f_7 \leftarrow f_7 - \frac{\dot{u}_x}{12} + \frac{\dot{u}_y}{12} \quad f_8 \leftarrow f_8 - \frac{\dot{u}_x}{12} - \frac{\dot{u}_y}{12} \quad f_9 \leftarrow f_9 + \frac{\dot{u}_x}{12} - \frac{\dot{u}_y}{12}$$

(Equation 4-5)

4.5 SUBCYCLING OF THE FLUID SOLVER

An important note regarding the coupling scheme is that the inherent high-frequency fluctuations in the LB fluid solver can artificially excite higher mode structural vibrations, as illustrated in Figure 4.4. These artificial high-frequency vibrations can degrade the accuracy of the simulation and can lead to instability. Time averaging of the fluid pressure has been shown to significantly reduce the effect of this artificial noise. This approach is particularly effective and efficient when the minimum time step required for the dynamic solid solver is significantly larger than the time step required for the LB fluid solver. The simulations developed for this study, for example, utilize a solid model where the time step required to capture the vibration modes of interest is an order of magnitude larger than the lattice time step. As a result, running the fluid and solid solvers on different time scales

(e,g. running the fluid solver at every lattice time step and the solid solver at every tenth lattice time step), and using a time-averaged pressure loading has two distinct advantages: (1) reduction of high-frequency noise in the fluid solver and the resulting high-frequency structural excitation, and (2) computational efficiency since the solid solver is only executed at a frequency required to capture the modes of interest. The effect of this time-averaging approach, however, should be investigated against benchmark data to ensure an accurate and stable solution.

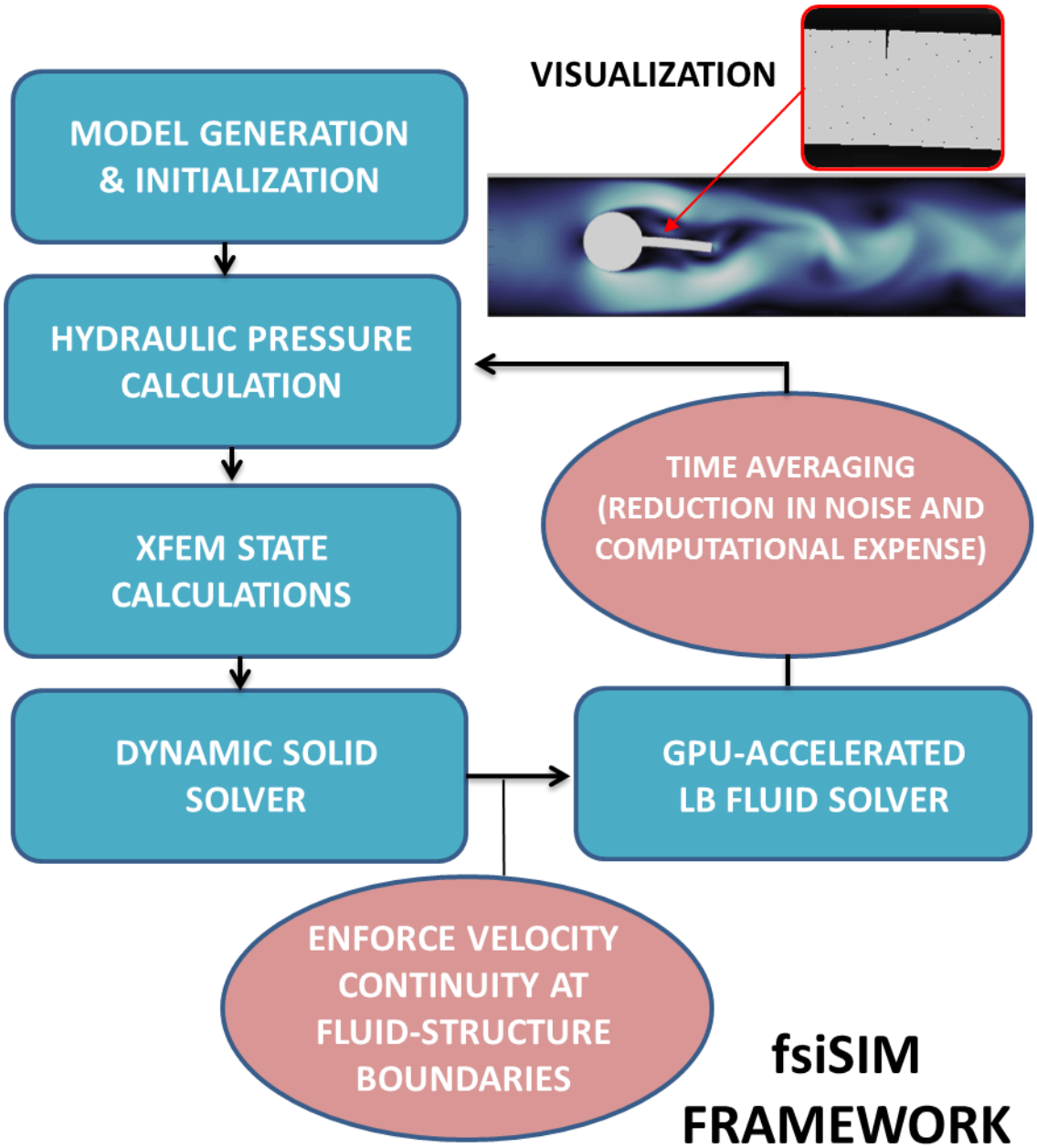

Figure 4.1. Simulation flowchart

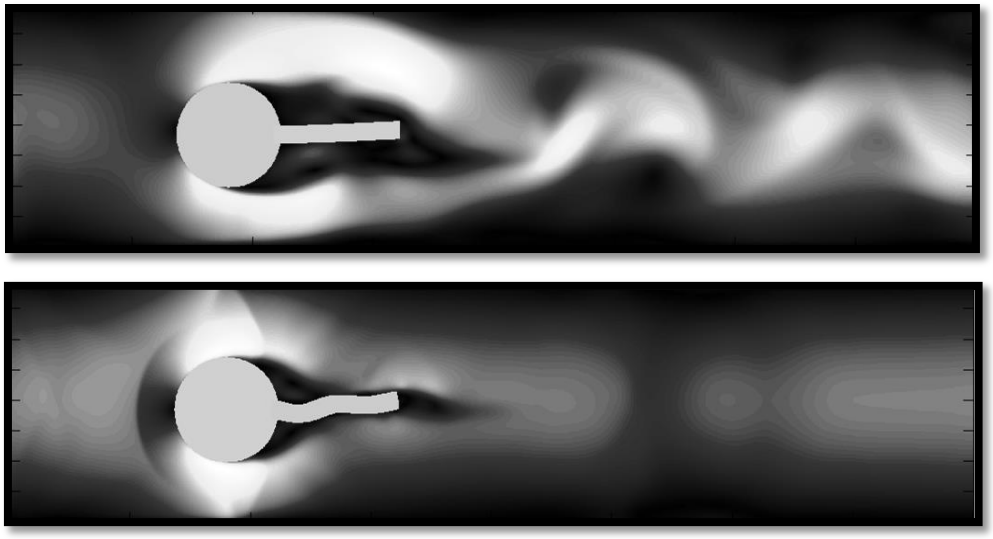

Figure 4.2. FSI simulations for a beam excited by vortex-induced vibration: (a) stiff case (higher elastic modulus) and (b) flexible case (lower elastic modulus)

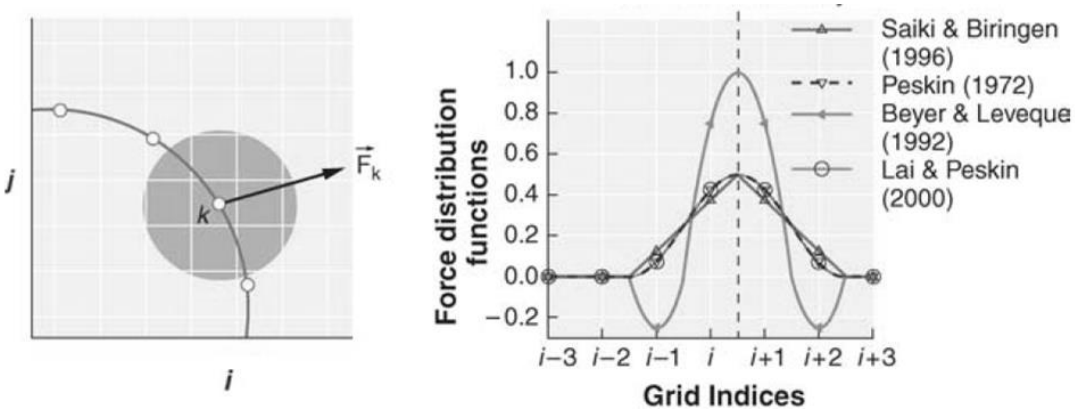

Figure 4.3. Distribution functions (Mittal and Iaccarino, 2005)

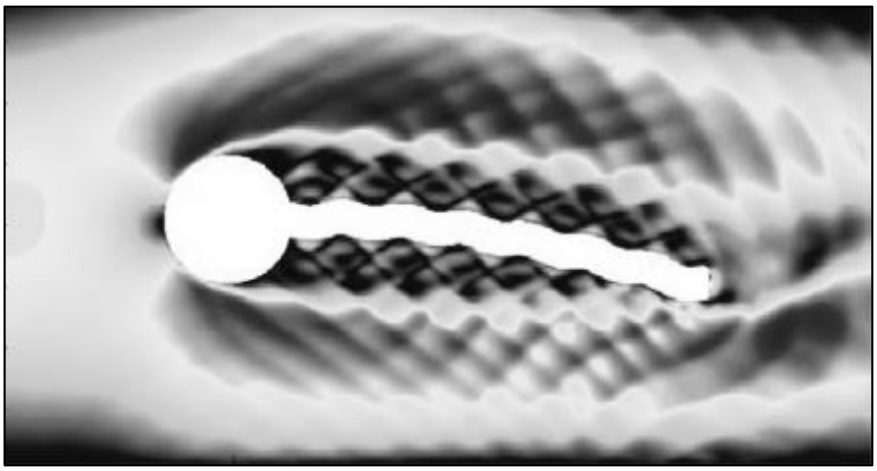

Figure 4.4. Artificial excitation of higher mode structural response due to inherent fluctuations in the LB fluid solver

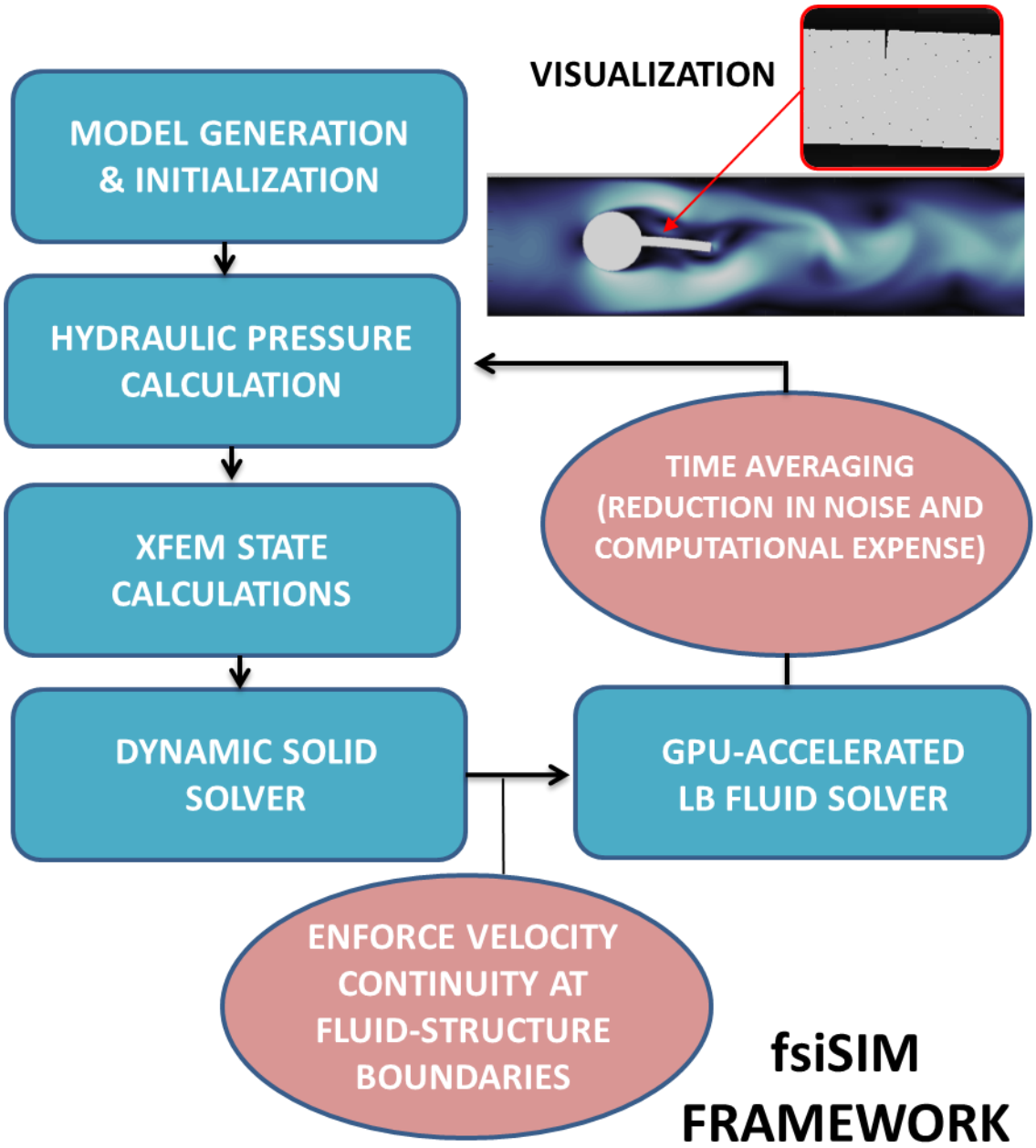

Figure 4.1. Simulation flowchart

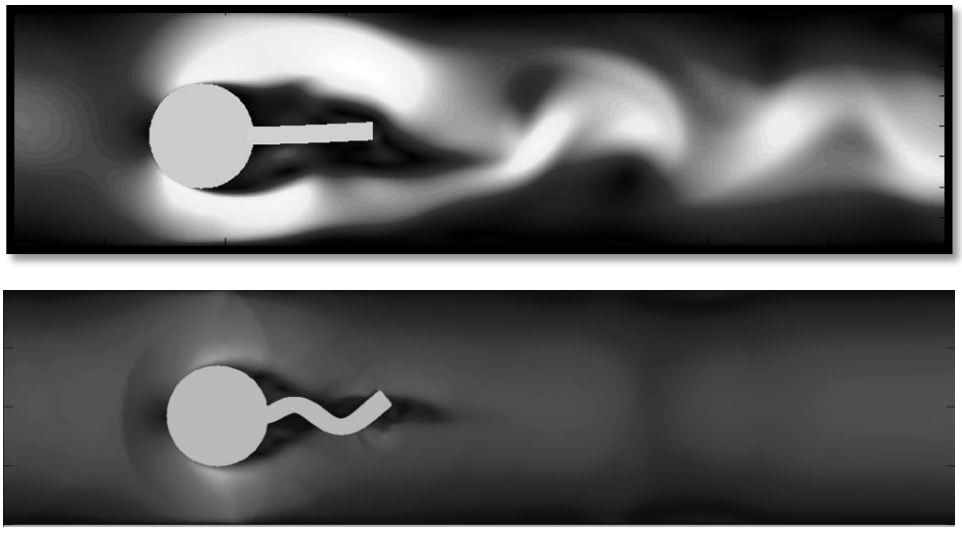

Figure 4.2. FSI simulations for a beam excited by vortex-induced vibration: (a) stiff case (higher elastic modulus) and (b) flexible case (lower elastic modulus)

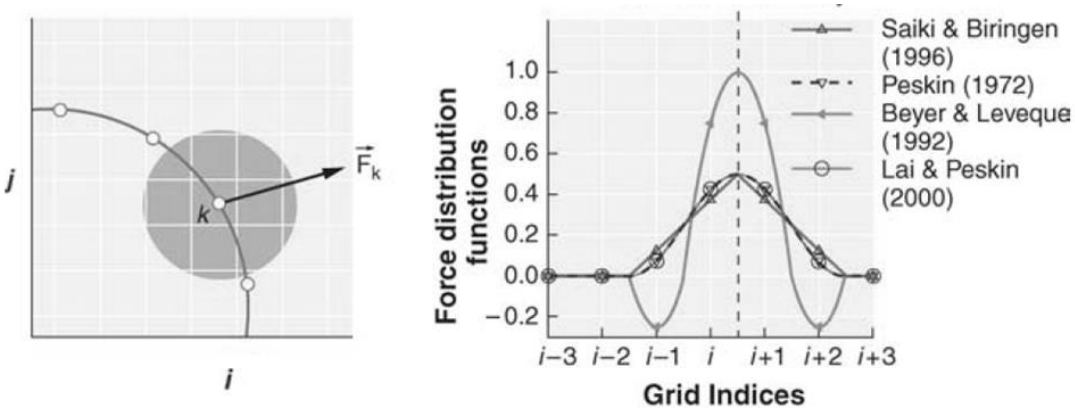

Figure 4.3. Distribution functions (Mittal and Iaccarino, 2005)

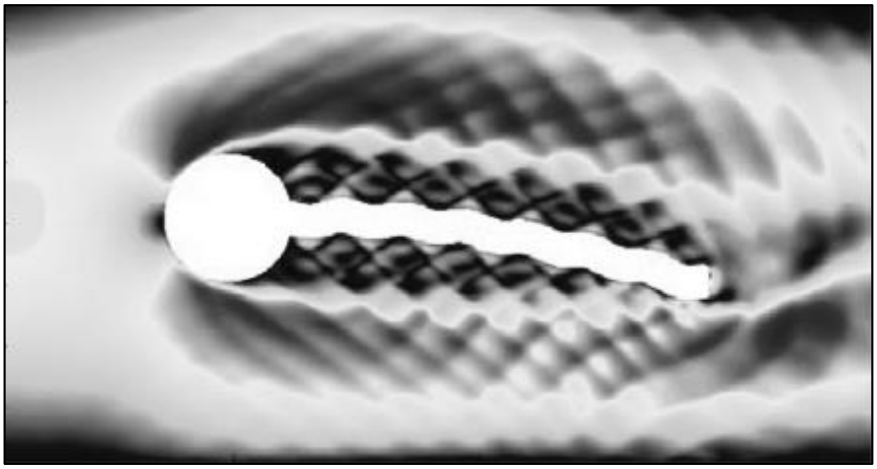

Figure 4.4. Artificial excitation of higher mode structural response due to inherent fluctuations in the LB fluid solver

CHAPTER 5

BENCHMARK SIMULATIONS

5.1 FLUID-STRUCTURE INTERACTION

A 2-D FSI simulation benchmark developed by Turek and Hron (2006) was utilized to validate the code for large-displacement FSI response. A schematic illustration of the problem is provided in Figure 5.1 (denoted as case FSI3 in Turek and Hron (2006)). Similar to previous examples presented in this paper, the benchmark simulation considered a flexible beam immersed in steady channel flow, such that the beam is excited by vortex shedding from the rigid circular obstruction to which it is attached. The channel is 41cm wide by 250 cm long with a peak inlet velocity of 2 m/s. The fluid has a density of 1000 kg/m^3 and a kinematic viscosity of 0.001 m^2/s. The flexible beam is 35 cm long by 2 m thick, and is constructed of a material with a density of 1000 kg/m^3, a Poisson ratio of 0.4, and an elastic modulus of 5.6 MPa. The beam is oriented in the direction of the flow and is attached to a rigid circular obstruction of diameter 10 cm. The center of the circular obstruction is located 20 cm from the inlet and 20 cm from the upper wall. Non-slip conditions were assumed for both wall boundaries. The Reynolds number for the flow, based on a characteristic length equal to the diameter of the circular obstruction, was 200.

The LB fluid solver was run on a D2Q9 lattice with a grid resolution of 1 mm and a time step of 0.1 ms. For computational efficiency, the BGK algorithm was utilized with the relaxation parameter τ set to 0.83. For consistency, the flexible beam was discretized to match the resolution of the fluid solver (20 elements in the through thickness direction).

Quadrilateral plane strain continuum elements with 2x2 Gauss quadrature were utilized. In order to reduce the effect of numerical noise in the fluid solver, and to improve computational efficiency, the fluid solver was subcycled relative to the solid solver by a factor of 10 (as discussed in Chapter 4) and hydraulic pressures at the fluid-solid boundary were time averaged. In addition, structural damping was included in the form of Rayleigh mass and stiffness proportional damping with 1% of critical in the first and second modes of vibration.

The BGK simulation produced a lateral beam tip displacement of 3-4 cm at an average frequency of 4-5 Hz. Figure 5.2 shows a snapshot of the deformed geometry of the beam and the velocity field, along with a time history plot of lateral beam tip displacement. These simulation results compare relatively well with the benchmark data of 3.4 cm and 5.3 Hz.

5.3 CRACK TIP STRESS INTENSITY

Prediction of crack tip stress intensity was compared with linear elastic fracture mechanics (LEFM) theory for two load configurations: (1) an edge cracked plate under remote uniaxial tension (pure mode I response), and (2) an asymmetric four-point bending configuration (mixed-mode response). Schematic illustrations of the load configurations are presented in Figure 5.3. In both cases, the simulations were run using quadrilateral plane strain continuum elements with 2x2 gauss quadrature. For the subdivided elements along the crack path, three gauss points were utilized for each triangular region within an element completely cut by the crack, and seven gauss points were utilized for the element

containing the crack tip. The theoretical mode I SIF for the edge cracked plate under remote uniaxial loading is given by Tada et al. (2000), and is presented in Equation 5-1.

$$K_I = \sigma_o \sqrt{\pi a}\, f(\lambda), \quad \lambda = a/W,$$

$$f(\lambda) = \frac{1}{\sqrt{\pi}}\left[\, 1.99 - 0.41\lambda + 18.70\lambda^2 - 38.48\lambda^3 + 53.85\lambda^4 \,\right]$$

(Equation 5-1)

In (Equation 5-1), σ_o is the remote uniaxial stress demand, W is the plate width, and a is the crack length. For a scenario where σ_o is equal to 1 MPa, W is 25 mm, and a is 2.5 mm, the theoretical mode I SIF is 1.1 MPa-m$^{1/2}$. Run for static loading with a mesh resolution of 1.25 mm, the XFE solver calculates a mode I SIF of 1.0 MPa-m$^{1/2}$ with a negligible mode II contribution of 3.8 kPa-m$^{1/2}$. Figure 5.4(a) presents the von Mises stress distribution, which includes a high intensity region around the crack tip.

The theoretical mode I and II SIFs for the four-point bending configuration are given by He and Hutchinson (2000), and are presented in Equations 5-2 and 5-3, respectively.

$$K_I = \frac{6cQ}{W^2}\sqrt{\pi a}\, F_I\left(\frac{a}{W}\right)$$

$$F_I\left(\frac{a}{W}\right) = 1.122 - 1.121\left(\frac{a}{W}\right) + 3.740\left(\frac{a}{W}\right)^2 - 19.05\left(\frac{a}{W}\right)^4 + 22.55\left(\frac{a}{W}\right)^5$$

(Equation 5-2)

$$K_{II} = \frac{Q}{W^{1/2}} \frac{\left(\frac{a}{W}\right)^{3/2}}{\left(1 - \frac{a}{W}\right)^{1/2}} F_{II}\left(\frac{a}{W}\right)$$

$$F_{II}\left(\frac{a}{W}\right) = 7.264 - 9.37\left(\frac{a}{W}\right) + 2.74\left(\frac{a}{W}\right)^2 + 1.87\left(\frac{a}{W}\right)^3 - 1.04\left(\frac{a}{W}\right)^4$$

(Equation 5-3)

In Equations 5-2 and 5-3, Q is given by Equation 5-4.

$$Q = \frac{P(b_2 - b_1)}{(b_2 + b_1)}$$

(Equation 5-4)

For a scenario where P is equal to 1.2 MN; b_1 and b_2 are 12.5 mm and 62.5 mm, respectively; W is 25 mm; a is 2.5 mm; and c is 0.625 mm, the theoretical mode I and mode II SIFs are 0.45 MPa-m$^{1/2}$ and 1.1 MPa-m$^{1/2}$, respectively. The corresponding XFE calculations for a mesh resolution of 0.625 mm are 0.48 MPa-m$^{1/2}$ and 1.3 MPa-m$^{1/2}$, respectively. The von Mises stress distribution is shown in Figure 5.4(b). The contour plot shows high stress demand along a narrow banded diagonal between the interior loading points, which is indicative of shear loading.

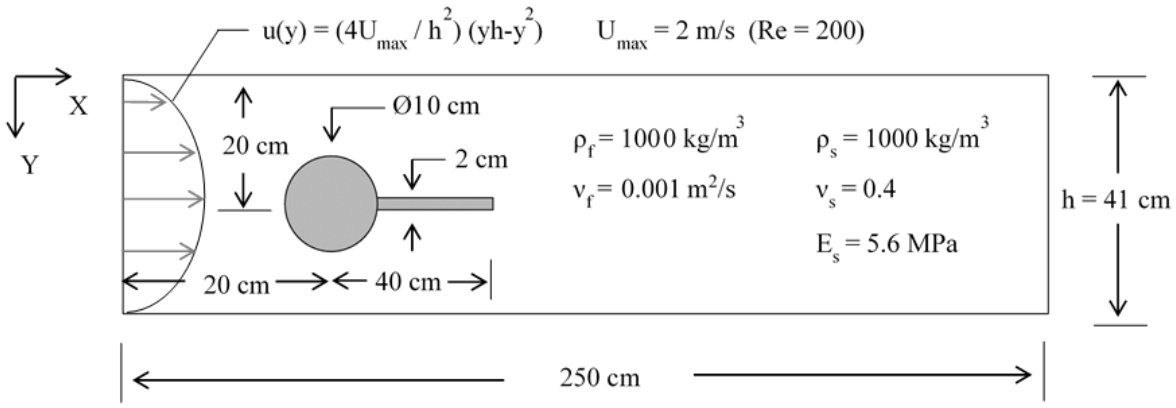

Figure 5.1. FSI benchmark simulation

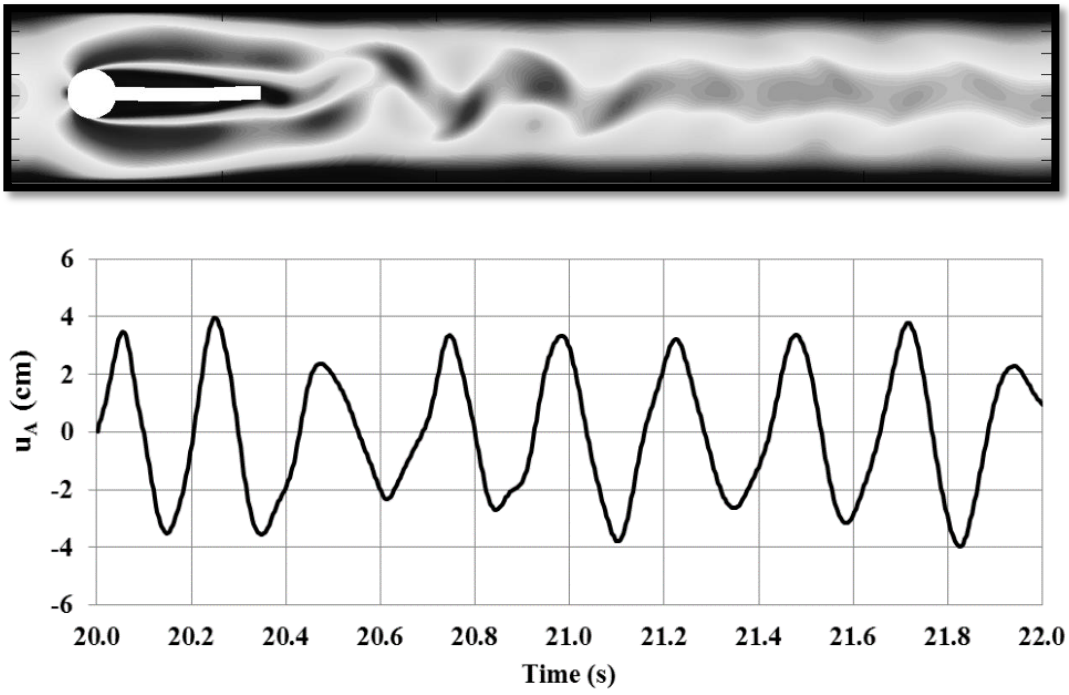

Figure 5.2. Beam tip displacement response for the BGK simulation

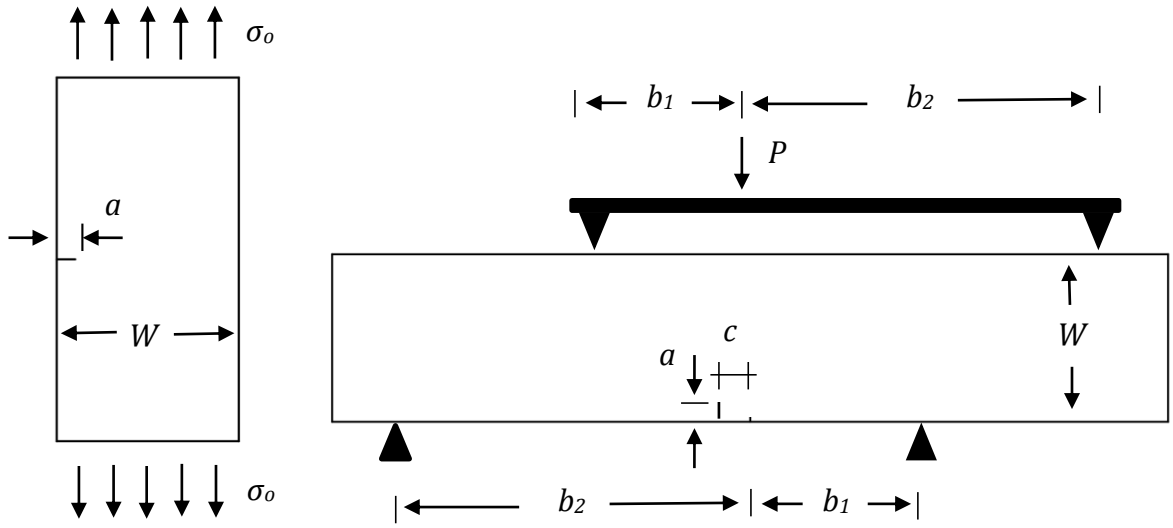

Figure 5.3. Crack tip stress intensity benchmark simulations:
(a) edge cracked plate under remote uniaxial tension (pure mode I response),
and (b) four-point bending configuration (mixed-mode response)

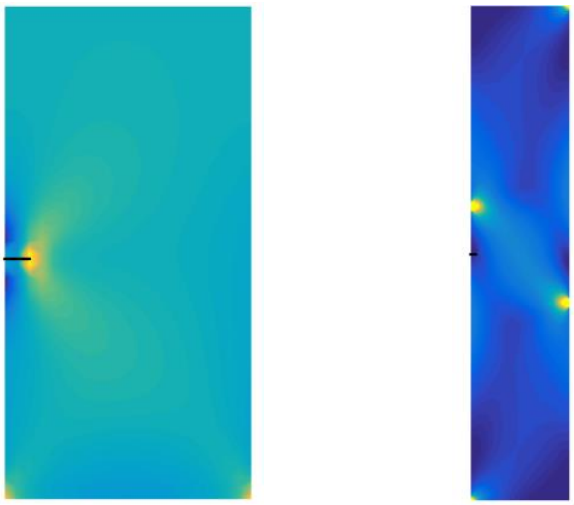

Figure 5.4. von Mises stress distribution:
(a) edge cracked plate under remote uniaxial tension (pure mode I response),
and (b) four-point bending configuration (mixed-mode response)

CHAPTER 6

DEMONSTRATION PROBLEM

6.1 NUMERICAL MODEL

In order to demonstrate the application of the LB-XFE modeling approach to fatigue life prediction and to developing/evaluating SHM schemes for crack detection, a simple 2-D case study was developed for a flexible beam subject to vortex-induced vibration. The case study was similar in form to the aforementioned FSI benchmark simulation but incorporated geometric and material property modifications in order to investigate a broader range of vibration characteristics during crack propagation. As shown in Figure 6.1, the model consisted of a 25 cm long by 2.5 cm thick beam connected to a 20 cm diameter rigid circular obstruction (fixed in space). The beam was immersed in a 50 cm wide by 200 cm long channel with a maximum inlet velocity of 2 m/s and an apparent Re of 236, based on a characteristic length equal to the diameter of the obstruction. The material properties for the solid and fluid domains, which are presented in Figure 6.1, are representative of an industrial plastic (e.g. polypropylene) and a viscous fluid (e.g. glycerin), respectively, but it is noted that the case study is intended to be arbitrary in nature (i.e. not representative of a particular real world application).

The LB fluid solver was run on a 400 x 1600 D2Q9 lattice with a grid resolution of 1.25 mm and a time step of 0.14 ms, using the BGK relaxation scheme with τ equal to 0.81. In order to reduce the effect of numerical noise in the fluid solver, and to improve computational efficiency, the fluid solver was subcycled relative to the solid solver by a

factor of 10 (as discussed in Chapter 4) and hydraulic pressures at the fluid-solid boundary were time averaged.

The FE model for the flexible beam utilized quadrilateral plane strain continuum elements with 2x2 Gauss quadrature and enrichment for crack modeling. Twenty elements were used in the thickness direction with 200 element columns along the length of the beam. Subcritical crack growth was modeled using the idealized power law presented in Equation 3-5, considering a critical threshold SIF range (ΔK_{th}) of 0.1 MPa-m$^{1/2}$ and fitting parameters (C, m) equal to 3x10^{-11} MPa-m$^{1/2}$ and 3, respectively. For the subdivided elements along the crack path, three Gauss points were utilized for each triangular region within an element completely cut by the crack, and seven Gauss points were utilized for the element containing the crack tip. The implicit nonlinear Newmark average acceleration method was used to integrate the dynamic equations of motion, considering Rayleigh damping with 1% of critical in the first and second modes of vibration (preserved throughout the simulation by updating the proportionality coefficients following each nonlinear event).

The simulation was run for 10 seconds before a 1 mm edge crack was instantaneously introduced along the upper surface, located 5 cm from the fixed base. The crack was allowed to propagate during the simulation according the specified growth law, as illustrated in Figure 6.2. Transverse accelerations in the beam were monitored at quarter points along the length, designated as virtual sensor locations L/4, 3L/4, and L (Figure 6.3). These acceleration records were then integrated to obtain the displacement histories at the

virtual sensor locations (Figure 6.4). Stress intensity at the crack tip and crack length were also recorded during the simulation.

6.2 TRANSVERSE MOTION

Transverse accelerations and displacements recorded for the uncracked condition are presented in Figures 6.5 and 6.6, respectively. As shown in Figure 6.6, the displacement response is dominated by the vortex shedding (forcing) frequency (2.3 Hz), but also includes a higher frequency component associated with the fundamental mode of vibration for the beam (32 Hz). The vortex shedding frequency f_v is calculated according to Equation 6-1.

$$f_v = \frac{St \cdot U_{max}}{D}$$

(Equation 6-1)

In Equation 6-1, St is the dimensionless Strouhal number, U_{max} is the peak free-stream velocity, and D is the diameter of the circular obstruction.

The effect of cracking on the transverse accelerations and displacements of the beam is illustrated in Figures 6.7 and 6.8, which present the respective measurements between 18 and 19 s into the simulation. During this snapshot in time, the crack extends 7-8.5 mm into the beam. The resulting softening of the beam brings the fundamental frequency of vibration closer to the forcing (vortex shedding) frequency and amplifies both the displacements and accelerations due to greater transmissibility. This cracking also

elongates the vibration periods of the beam, which, in turn, alters the vibration response to the forcing function. As will be shown in Section 6.4, this change in vibration frequency can be used to identify the presence of the crack through signal-based SHM methods. By 22 s into the simulation, crack-induced softening of the beam triggers a terminal instability.

6.3 STRESS INTENSITY AND CRACK EXTENSION

As noted earlier, the practical value of the modeling approach is in its ability to improve fatigue vulnerability assessment, and to evaluate crack detection schemes. By tracking demand measures like stress intensity at the crack tip (Figure 6.9) and crack extension (Figure 6.10), the modeling approach can be utilized in a reliability-based framework (through robust parametric studies) for evaluating the risk associated with fatigue cracking, as well as for estimating the lifespan of the structure. For example, a simulation-based fatigue assessment evaluation could consider variations in flow conditions, crack growth behavior, and defects. This information would be useful in the assessment of existing structures and for the design of new structures for FSI applications (e.g. evaluation of defect tolerance and critical flow conditions).

It is worth noting that stress intensity at the crack tip increases during the simulation due to greater transmissibility between the forcing function (vortex shedding) and the vibrating beam, which is attributed with crack-induced softening of beam lateral load response. As a result, crack growth is nonlinear due to the increase in time each cycle that crack opening is driven by tensile stress demands. Both stress intensity and crack length increase rapidly prior to the onset of numerical instability.

6.4 DEVELOPMENT AND ASSESSMENT OF STRUCTURAL HEALTH MONITORING SCHEMES FOR CRACK DETECTION

As an illustration of the utility of the modeling approach in the development and assessment of SHM schemes for crack detection, an autoregressive (AR) model was used to fit the transverse beam tip displacement data and a Cosh spectral distance damage feature (Wei and Gibson, 2000; Yao et al. 2012) was used to evaluate crack detection sensitivity. This signal-based approach to crack detection involves measuring the variation in the response (e.g. the transverse beam tip displacement) from a known baseline (healthy or uncracked condition). Since the recorded data is a collection of discrete points, regression models are employed to develop best-fit functions for statistical comparison. AR models are a particular classification of regression model that relate the current value of a predicted time series to past values of the same series, as defined by Equation 6-2.

$$y_j(t) = \sum_{p=1}^{P} \alpha_p y_j(t-p) + \varepsilon_y(t)$$

(Equation 6-2)

In Equation 6-2, α_p are the model coefficients, y_j is the output at location j, $\varepsilon_y(t)$ is the model residual, t is the time index, and P is the model order.

The Cosh spectral distance feature $C(S, \bar{S})$ is defined in Equation 6-3 and quantifies the change in spectral peaks, where a larger change is indicative of a change in structural condition (i.e. damage).

$$C(S,\bar{S}) = \frac{1}{2N}\sum_{j=1}^{N}\left[\frac{S(\omega_j)}{\bar{S}(\omega_j)} - log\frac{S(\omega_j)}{\bar{S}(\omega_j)} + \frac{S(\omega_j)}{\bar{S}(\omega_j)} - log\frac{S(\omega_j)}{\bar{S}(\omega_j)} - 2\right]$$

(Equation 6-3)

In Equation 6-3, $\bar{S}(\omega_j)$ is the mean baseline spectra, $S(\omega_j)$ is unknown state spectrum, and N is the length of each spectrum vector.

Since the transverse motion of the beam is dominated by the fundamental mode of response, as evidenced by the correlation between displacement peaks recorded at the virtual sensor locations (Figures 6.6 and 6.8), only the beam tip displacement data was utilized for the crack detection study. Figure 6.11 presents the time evolution of the Cosh spectral distance damage feature for a model order of 2. Each recording is representative of a 3 s snapshot sampled at 710 Hz. The healthy baseline measurement was taken as the recording from 4-7 s seconds, and the control data (uncracked condition) presented in Figure 6.11 was recorded from 7-10 s. Figure 6.11 shows a progressive increase in the damage feature, corresponding to a greater likelihood of identifying the presence of the crack as a statistically significant deviation.

For this simple test case, cracks at least as small as 5% of the beam thickness can be identified through monitoring of the beam tip displacement and evaluating the Cosh spectral distance damage feature. For more complex structures, the type of measurement and the sensor array become more important, especially for applications where crack

location is of interest. Parametric studies facilitated by the proposed modeling approach can be used to optimize the monitoring approach for anticipated service conditions.

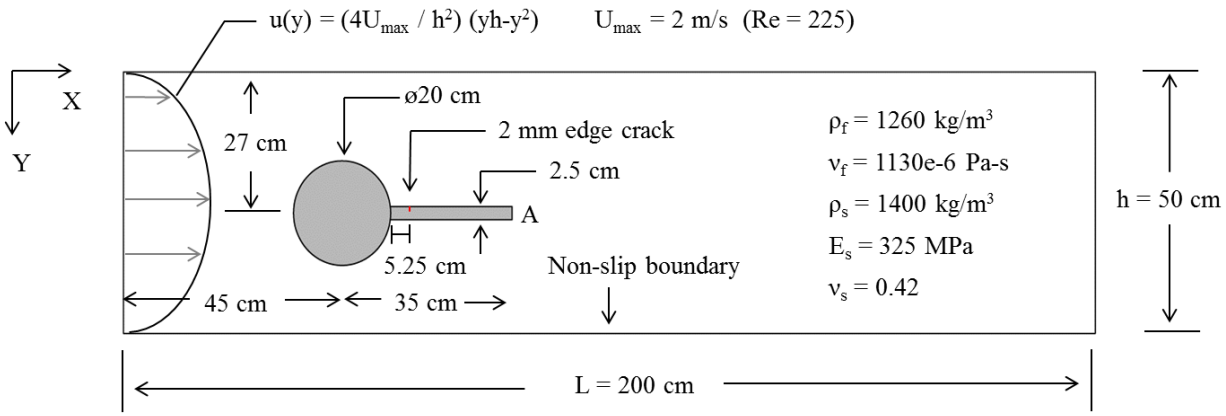

Figure 6.1. Demonstration problem: flexible beam excited by vortex-induced vibration

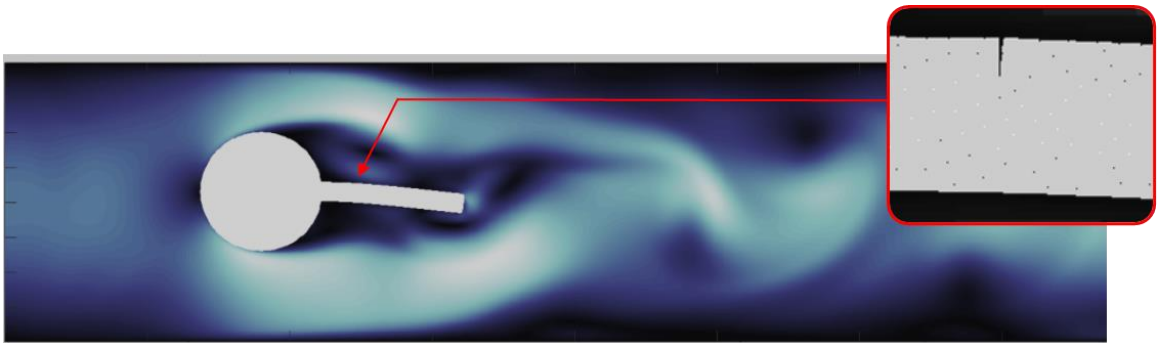

Figure 6.2. Crack growth during vortex-induced vibration

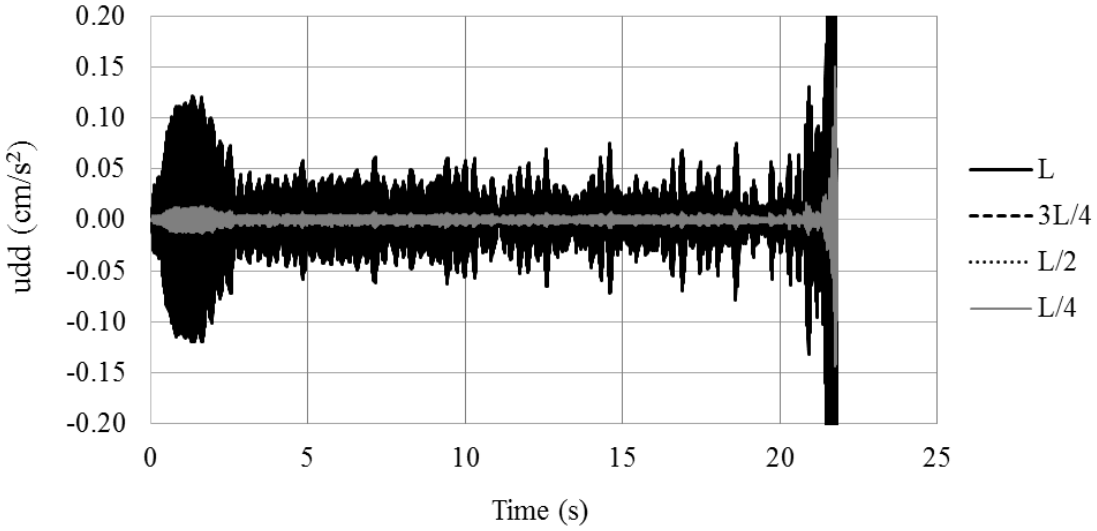

Figure 6.3 Virtual sensor transverse acceleration records

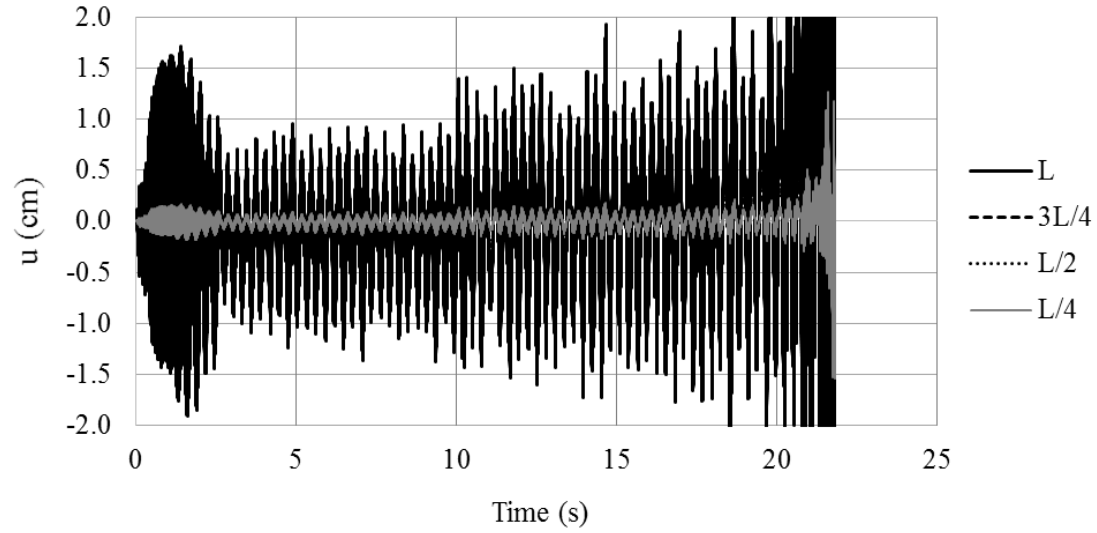

Figure 6.4. Virtual sensor transverse displacement records

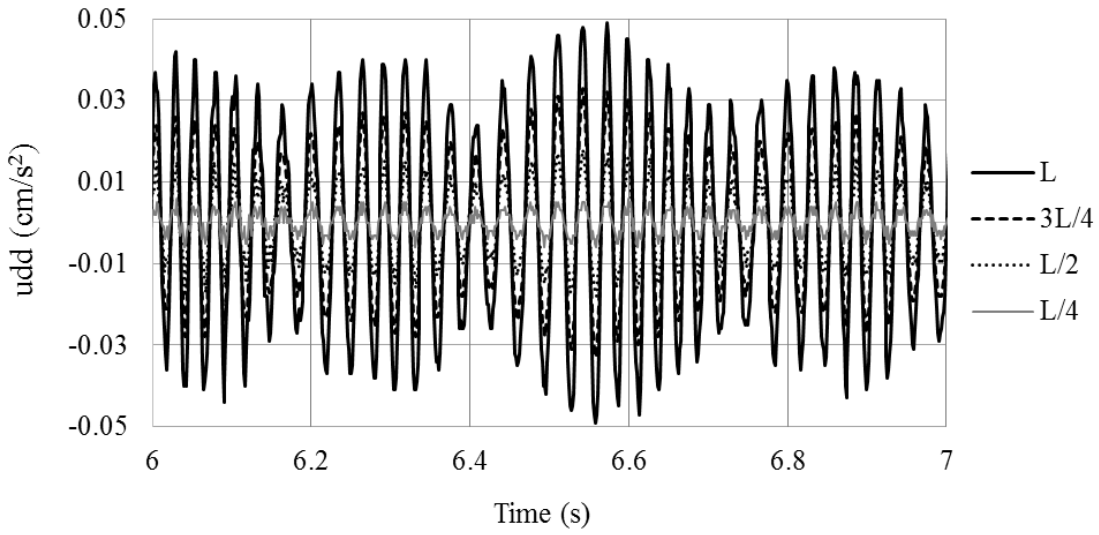

Figure 6.5 Virtual sensor transverse acceleration records from 6-7 s (uncracked condition)

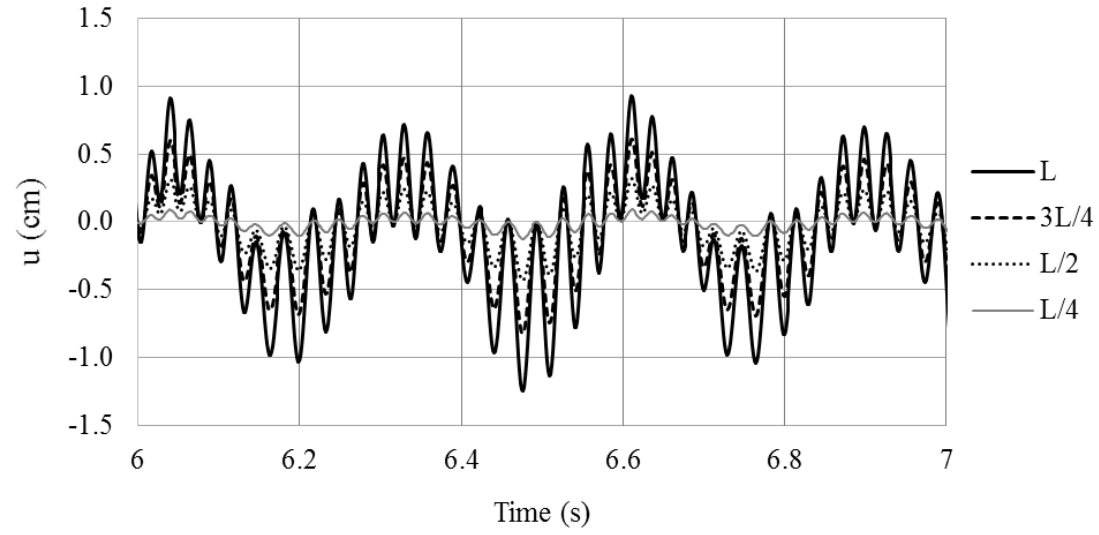

Figure 6.6 Virtual sensor transverse displacement records from 6-7 s (uncracked condition)

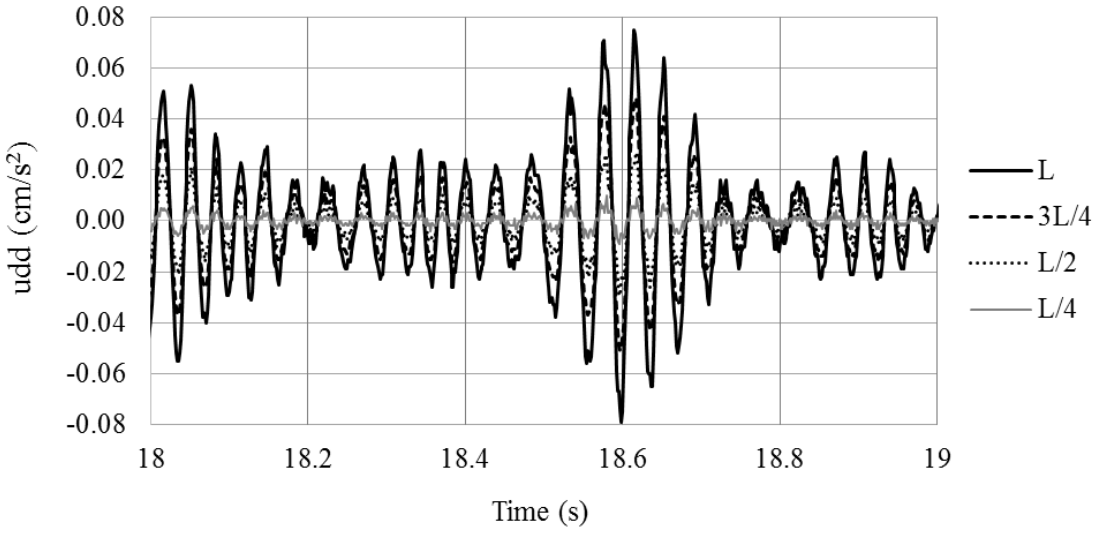

Figure 6.7 Virtual sensor transverse acceleration records from 18-19 s (7-8.5 mm crack)

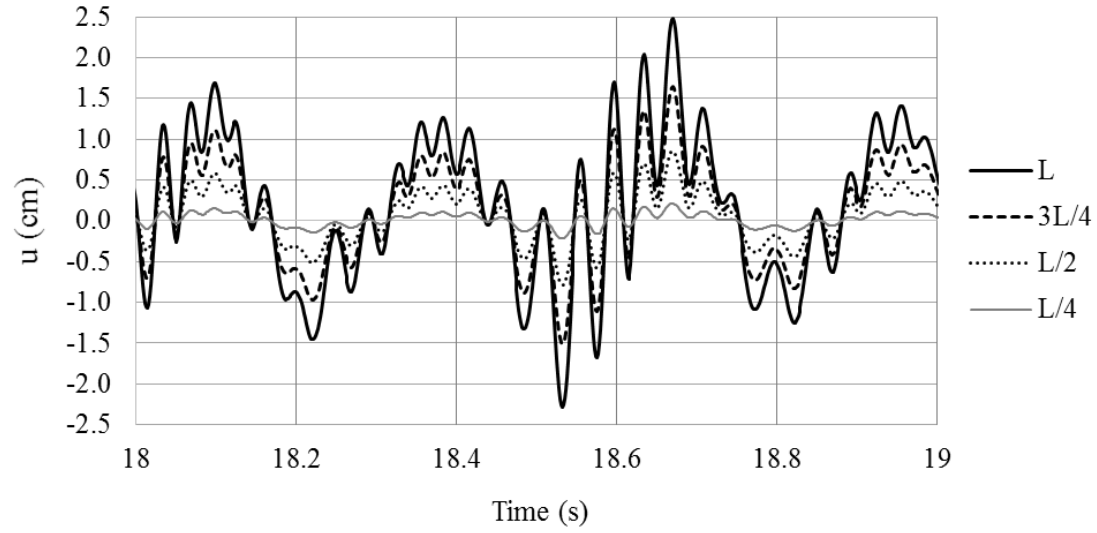

Figure 6.8 Virtual sensor transverse displacement records from 18-19 s (7-8.5 mm crack)

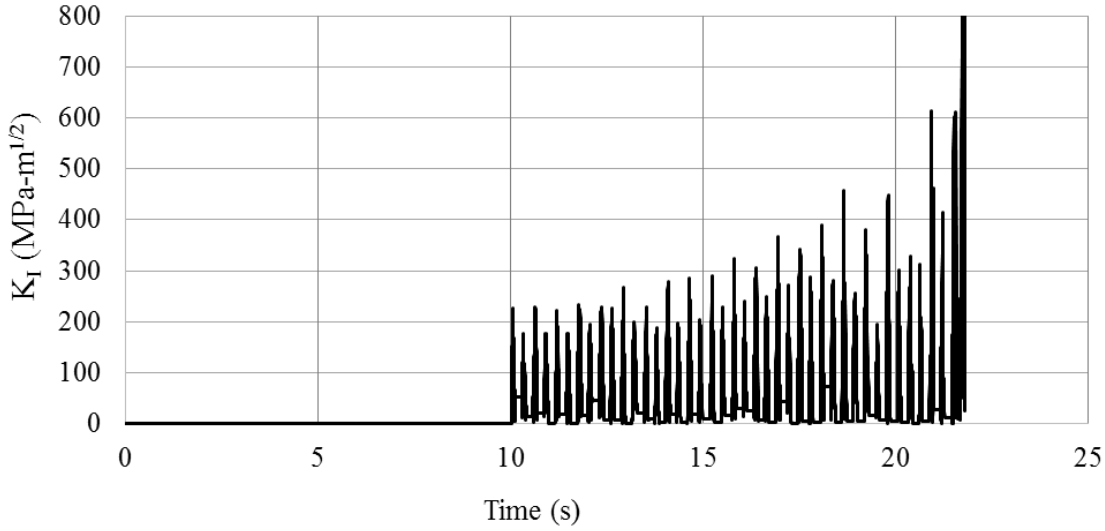

Figure 6.9 Mode I stress intensity

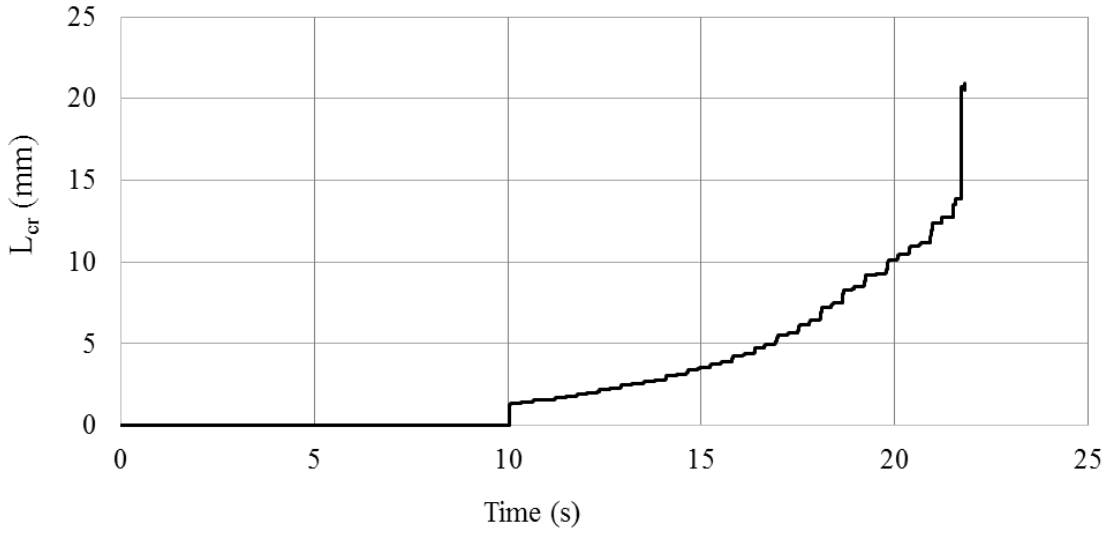

Figure 6.10 Crack length

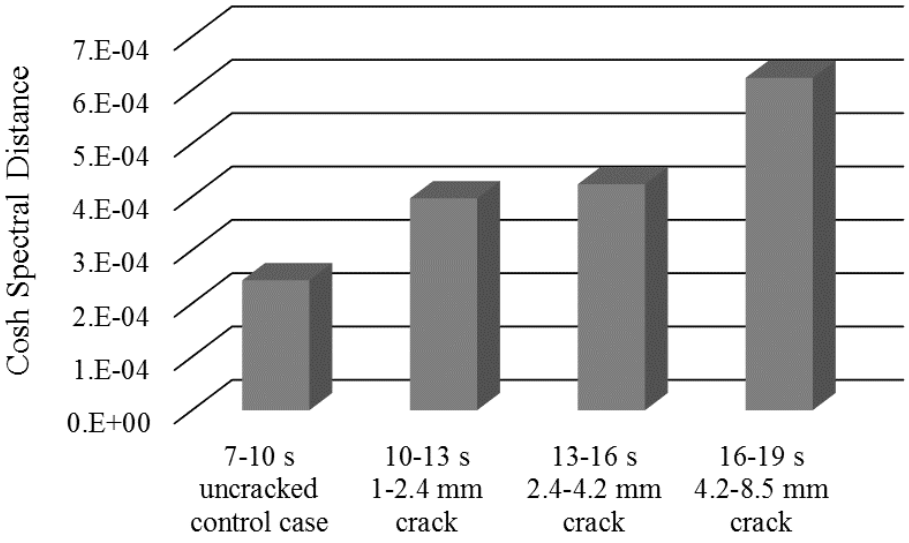

Figure 6.11. Time evolution of the Cosh spectral distance damage feature

CHAPTER 7

SUMMARY, CONCLUSIONS, AND FUTURE WORK

11.1 SUMMARY AND CONCLUSIONS

This study presented a modeling approach for fluid-structure interaction (FSI) simulation with dynamic crack propagation, with the objective of utilizing simulation-based parametric studies to improve fatigue life prediction and crack detection in FSI applications. The modeling approach pairs a GPU (graphics processing unit)-accelerated lattice Boltzmann (LB) fluid solver with an extended finite element (XFE) solid solver through an immersed boundary (IB) coupling scheme. The modeling approach takes advantage of several inherent features of the integrated solvers, namely: (1) scalable GPU parallelization of the LB fluid solver, as well as its ability to handle turbulent and multi-phase flows with relative ease (not implemented in this study); (2) the reduced mesh-dependence of the XFE method for modeling crack propagation; and (3) the ability of the IB coupling scheme to handle large-displacement response without global adaptive meshing. The coupled LB-XFE framework developed in this paper offers a versatile and computationally efficient approach for simulating FSI response with crack propagation.

For demonstration purposes, the modeling framework was used to develop a subcritical crack growth simulation for a flexible beam subject to vortex-induced vibration. The demonstration problem illustrates the utility of the modeling approach in its ability to track demand measures such as SIF at the crack tip and crack growth for fatigue vulnerability assessment, and in its ability to evaluate crack detection schemes.

The modeling approach, however, does have several limitations. Because of physical deficiencies with the LB fluid solver, simulations are restricted to low Mach flow (generally less than 0.2-0.3). In addition, the empirical fatigue crack growth model utilized by the XFE solver requires calibration. This calibration process is complicated for FSI applications due to physical conditions that violate many of the assumptions commonly utilized in fracture mechanics (e.g. hydraulic loading of the crack surface; surface contact during crack closure; and variable amplitude loading). The relative influence of these conditions should be investigated for a particular application.

11.4 FUTURE WORK

The following research tasks are proposed in order to extend the capability of the code to study more realistic applications:

- Extension to 3-D simulation by developing 3-D continuum and 3-D shell elements with crack modeling capability, noting that one of the strengths of the LB fluid solver is its ability to handle complex 3-D geometries.
- Full GPU-implementation of the code in order to improve efficiency.
- Implementation of turbulent flow and multi-phase flow modeling in the LB fluid solver.

REFERENCES

ACRIGS (2015) www.acrigs.com (accessed 10/2015).

Belytschko, T. and Black, T. (1999) "Elastic crack growth in finite elements with minimal remeshing," *International Journal for Numerical Methods in Engineering*, 45(5):601-620.

Belytschko, T. Gracie, R., Ventura, G. (2009) "A review of extended/generalized finite element methods for material modeling," *Modeling and Simulation in Materials Science and Engineering*, 17(4):1-24.

Bhatnagar, P.L., Gross, E.P. and Krook, M. (1954) "A model for collision processes in gases. I. Small amplitude process in charged and neutral one-component systems," *Physical Review,* 94:511-525.

Blair, S.R. (2012) "Lattice Boltzmann methods for fluid structure interaction," *Dissertation*, Department of Mechanical Engineering, Naval Postgraduate School, Monterey, CA.

Bordas, S., Nguyen, P.V., Dunant, C., Nguyen-Dang, H., and Guidoum, A. (2006) "An extended finite element library," *International Journal for Numerical Methods in Engineering*, 71(6):703-732.

Bouzidi, M., d'Humieres, D., Lallemand, P., and Luo, L. (2001) "Lattice Boltzmann equation on a two-dimensional rectangular grid," *Journal of Computational Physics*, 172: 704-717.

Cecrdle, J. (2015) *Whirl flutter of turboprop aircraft structures*, Woodhead Publishing, Waltham, MA.

Chirila, D.B. (2001) "Introduction to lattice Boltzmann methods," available from www.awi.de (accessed 5/2013).

Chopra, A.K. (2007) *Dynamics of structures*, Prentice Hall, Upper Saddle River, NJ.

d'Humieres, D. (1992) "Generalized lattice Boltzmann equations," *Prog. Aeronaut. Astronaut.*, 159:450-458.

d'Humieres, D., Ginzburg, I., Krafczyk, M., Lallemand, P., and Luo, L. (2001) "Multiple-relaxation-time lattice Boltzmann models in three dimensions," *Philosophical Transactions of the Royal Society A*, 360:437-451.

Fakhari, A. and Lee, T. (2013) "Multiple-relaxation-time lattice Boltzmann method for immiscible fluids at high Reynolds numbers," *Physical Review E*, 87: 023304(8).

Fleming, M., Chu, Y.A., Moran, B., and Belytschko, T. (1997) Enriched element-free Galerkin methods for crack tip fields," *International Journal for Numerical Methods in Engineering*, 40(8):1483-1504.

Fries, T. and Belytschko, T. (2010) "The extended/generalized finite element method: An overview of the method and its applications," *International Journal for Numerical Methods in Engineering*, 84(3):253-304.

Gorban, A.N. and Packwood, D.J. (2014) "Enhancement of the stability of lattice Boltzmann methods by dissipation control," *Physica A*, 414:285-299.

Guo, X., Zhong, C., Zhuo, C., and Cao, J. (2013) "Multiple-relaxation-time lattice Boltzmann method for study of two-lid-driven cavity flow solution multiplicity," *Theoretical and Computational Fluid Dynamics*, DOI 10.1007/s00162-013-0312-3.

He, X. and Doolen, G.D. (1997) "Lattice Boltzmann method on a curvilinear coordinate system: Vortex shedding behind a circular cylinder," *Physical Review E*, 56:434-440.

He, M.Y. and Hutchinson, J.W. (2000) "Asymmetric four-point crack specimen," *Journal of Applied Mechanics*, 67:207-209.

Hilber, H.M., Hughes, T.J.R., and Taylor, R.L. (1977) "Improved numerical dissipation for time integration algorithms in structural dyanmics," *Earthquake Engineering and Structural Dyanmcis*, 5:282-292.

Huang, C. (2012) "Structural health monitoring system for deepwater risers with vortex-induced vibration," *Dissertation*, Rice University, Houston, TX.

Jacobs, T.S., Won, J., Gravereaux, E.C., Faries, P.L., Morrissey, N., Teodorescu, V.J., Hollier, L.H., and Marin, M.L. (2003) "Mechanical failure of prosthetic human implants: a 10-year experience with aortic stent graft devices," *Journal of Vascular Surgery*, 37(1):16-26.

Karihaloo, B.L. and Xiao, Q.Z. (2003) "Modelling of stationary and growing cracks in FE framework without remeshing: A state-of-the-art review," *Computers and Structures*, 81(3):119-129.

Kruger, T., Fathollah, V., and Raabe, D. (2009) Shear stress in lattice Boltzmann simulations," *Physical Review E*, 79(4):046704(14).

Kwon, Y.W. (2006) "Development of coupling technique for LBM and FEM for FSI application," *International Journal for Computer-Aided Engineering and Software*, 23(8):860-875.

Lallemand, P. and Luo, L. (2000) "Theory of the lattice Boltzmann method: dispersion, dissipation, isotropy, Galilean invariance, and stability," *ICASE Report No. 2000-17*, NASA Langley Research Center, Hampton, VA.

Maier, R.S., Bernard, R.S., and Grunau, D.W. (1996) "Boundary conditions for the lattice Boltzmann method," *Physics of Fluids*, 8(7):1788-1801.

Menouillard, T., Rethore, J., Combescure, A., and Bung, H. (2006) "Efficient explicit time stepping for the extended finite element method (X-FEM)," *International Journal for Numerical Methods in Engineering*, 68(9):911-939.

Moes, N., Dolbow, J.E., and Belytschko, T. (1999) "A finite element method for crack growth without remeshing," *International Journal for Numerical Methods in Engineering, 46(1):131-150.*

Mohammadi, S. (2008) *Extended finite element method*, Blackwell Publishing Ltd., Oxford, UK.

Nikishkov, G.P. and Atluri, S.N. (1987) "Calculation of fracture mechanics paramters for an arbitrary three-dimensional crack by the equivalent domain integral method," *International Journal for Numerical Methods in Engineering*, 24(9):1801-1821.

Osher, S. and Sethian, J. (1988) "Fronts propagating with curvature-dependent speed: algorithms based on Hamilton-Jacobian formulations," *Journal of Computational Physics*, 100(2):209-228.

Pais, M.J. (2011) “Variable amplitude fatigue analysis using surrogate models and exact XFEM reanalysis,” *Dissertation*, Department of Mechanical Engineering, University of Florida, Gainesville, FL.

Paris, P., Gomez, M., and Anderson, W. (1961) “A rationale analytic theory of fatigue,” *The Trend in Engineering*, 13:9-14.

Peskin, C.S. (2002) “The immersed boundary method,” *Acta Numerica*, 1-39.

Rice, J. (1968) “A path independent integral and the approximate analysis of strain concentration by notches and cracks,” *Journal of Applied Mechanics*, 35(2):379-386.

Riveros, C., Utsunomiya, T., Maeda, K., and Itoh, K. (2007) “Vibration-based damage detection in flexible risers using time series analysis,” *Doboku Gakkai Ronbunshuu A*, 63(3):423-433.

Sanford, R.J. (2003) *Principles of fracture mechanics*, Prentice Hall, Upper Saddle River, NJ.

Sih, G.C. (1974) “Strain-energy-density factor applied to mixed mode crack problems,” *International Journal of Fracture*, 10(3):305-321.

Suci, S. (2001) *The lattice Boltzmann equation for fluid dynamics and beyond*, Clarendon Press, Oxford, UK.

Sukumar, N., Dolbow, J.E., Devan, A., Yvonnet, J., Chinesta, F., Ryckelynck, D., Lorong, P., Alfaro, I., Martinez, M.A., Cueto, E., and Doblare, M. (2005) “Meshless methods and partition of unity finite elments,” *International Journal of Forming Processes*, 8(4):409-427.

Tada, H., Paris, P.C., and Irwin, G.R. (2000) *The stress analysis of cracks handbook*, ASME Press, New York, NY.

Turek, S. and Hron, J. (2006) “Proposal for numerical benchmarking of fluid-structure interaction between an elastic object and laminar incompressible flow,” *Lecture Notes in Computational Science and Engineering, Fluid-Structure Interaction*, 53:246-260.

Wei, B. and Gibson, J.D. (2000) “Comparison of distance measures in discrete spectral modeling,” Proceedings from IEEE Digital Signal Processing Workshop, 1-4.

Westergaard, I. (1939) “Bearing pressures and cracks,” *Journal of Applied Mechanics*, 6(1):49-53.

Williams, M. (1957) “On the stress distribution at the base of a stationary crack,” *Journal of Applied Mechanics*, 24(1):109-114.

Yazid, A., Abdelkader, N., Adbelmadjid, H. (2009) “A state-of-the-art review of the X-FEM for computational fracture mechanics,” *Applied Mathematical Modeling*, 33(12):4269-4282.

Yao, R. and Pakzad, S.N. (2012) “Autoregressive statistical pattern recognition algorithms for damage detection in civil structures,” *Mechanical Systems and Signal Processing*, 31:355-368.

Zhou, Q. and He, X. (1997) “On pressure and velocity boundary conditions for the lattice Boltzmann BGK model,” *Physics of Fluids* 9(6):1591-1598.

VITA

Wesley John Keller graduated from Washington and Lee University in 2002 with a B.S. in Engineering Physics. He earned a M.S. in Civil Engineering from Virginia Tech University in 2004 and a Ph.D. in Structural Engineering from Lehigh University in 2012. He is a licensed Professional Engineer in California and Pennsylvania, and is a member of the Tau Beta Pi National Engineering Society and the Sigma Xi National Scientific Research Society. In 2010, he was a National Science Foundation sponsored Visiting Research Scientist at the Hyogo Earthquake Engineering Research Center (E-Defense) in Hyogo, Japan. He is currently employed as a Structural/Mechanical Analyst in the Computational Engineering Division of Lawrence Livermore National Laboratory.